

## Inclusive production of multistrange hyperons from 11-GeV/c $K^-p$ interactions

D. Aston,<sup>a</sup> R. K. Carnegie,<sup>b</sup> W. Dunwoodie,<sup>a</sup> S. Durkin,<sup>a\*</sup> P. G. Estabrooks,<sup>b</sup> R. J. Hemingway,<sup>b</sup> A. Honma,<sup>a†</sup>  
 D. Hutchinson,<sup>a</sup> W. B. Johnson,<sup>a</sup> P. F. Kunz,<sup>a</sup> T. Lasinski,<sup>a‡</sup> D. W. G. S. Leith,<sup>a</sup> L. Levinson,<sup>a§</sup> R. McKee,<sup>a\*\*</sup>  
 B. T. Meadows,<sup>d</sup> A. C. McPherson,<sup>b</sup> W. T. Meyer,<sup>a††</sup> G. K. Oakham,<sup>b†</sup> B. N. Ratcliff,<sup>a</sup> S. Shapiro,<sup>a</sup>  
 T. Shimomura,<sup>a</sup> S. Suzuki,<sup>a‡‡</sup> J. Va'Vra,<sup>a</sup> and S. Williams<sup>a</sup>

<sup>a</sup>Stanford Linear Accelerator Center, Stanford University, P.O. Box 4349, Stanford, California 94305

<sup>b</sup>Carleton University, Ottawa, Ontario, Canada K1S 5B6

<sup>c</sup>National Research Council, Ottawa, Ontario, Canada K1A 0R6

<sup>d</sup>University of Cincinnati, Cincinnati, Ohio 45221

(Received 17 June 1985)

Large samples of inclusively produced  $\Xi^-$ ,  $\Omega^-$ , and  $\Xi^0(1530)$  events are presented from a 1427 events/ $\mu\text{b}$  exposure of the large-aperture superconducting-solenoid spectrometer to an 11-GeV/c  $K^-$  beam. Production characteristics of these states are compared with other data and shown to be consistent with hyperon exchange. Polarization of  $\Xi^-$  shows an increase in magnitude with both Feynman  $x$  and transverse momentum. The  $\Xi^-$  decay parameters are measured to be  $\alpha_{\Xi^-} = -0.40 \pm 0.03$  and  $\Phi_{\Xi^-} = (5 \pm 10)^\circ$ . Results of searches for higher-mass hyperons are presented. The  $\Xi^-(1820) \rightarrow \Xi^0(1530)\pi^-$  decay is observed, while we fail to confirm the existence of the  $\Sigma^+(3170)$ .

### I. INTRODUCTION

Very little data on the inclusive production and decay characteristics of baryons with strangeness  $-2$  or  $-3$  have been reported in the literature.  $K^-p$  interactions have been studied at a variety of momenta<sup>1-7</sup> from 4.2 to 16 GeV/c to reveal  $\Xi^-$  inclusive characteristics, but detailed studies of  $\Xi^0(1530)$  production data have been made only at 4.2 GeV/c (Ref. 1), at 8.25 GeV/c (Ref. 2), and, with very limited statistics, at 10 and 16 GeV/c (Ref. 3). The only study of  $\Omega^-$  inclusive production has been at 8.25 GeV/c (Ref. 2). Each of these sets of data has come from bubble-chamber experiments where the complex event topologies involved were readily recognized. Previous counter experiments have isolated large samples of  $\Xi^-$  and  $\Omega^-$  particles, but have mainly concentrated in studying either an entirely different production mechanism from hyperon-beam interactions with protons and deuterons,<sup>8</sup> or their weak decay modes,<sup>9-13</sup> and some discrepancies exist among these large experiments over the value of the  $\Xi^- \rightarrow \Lambda\pi^-$  decay asymmetry parameter.

In this paper, we describe results from the first phase of an on-going study of data including the three hyperon production reactions:

$$K^-p \rightarrow \Xi^- + \text{anything} \quad (12\,550 \text{ events}) \quad (1.1)$$

$$\rightarrow \Omega^- + \text{anything} \quad (96 \text{ events}) \quad (1.2)$$

$$\rightarrow \Xi^0(1530) + \text{anything} \quad (1110 \text{ events}) \quad (1.3)$$

using the large-aperture superconducting-solenoid (LASS) spectrometer.<sup>14</sup> The raw exposure for the data presented here was 1427 eV/ $\mu\text{b}$ , and after including the effects of the average acceptances for these reactions—about 10% for  $\Xi^-$ , 5% for  $\Omega^-$  and  $\Xi^0(1530)$ —compares favorably with the largest of the bubble-chamber experiments (with

a reported exposure of 150 events/ $\mu\text{b}$ ) in which samples of 8121  $\Xi^-$ , 2772  $\Xi^0(1530)$ , and 67  $\Omega^-$  were accumulated.<sup>2</sup>

The data presented here were accumulated by the LASS spectrometer equipped with spark chambers as vertex detectors and represent about 10% of the total accumulation of such events. The remaining data, not reported here, were taken after a major upgrade in LASS to replace spark chambers by proportional wire chambers with a resolution approximately three times better. These latter data are presently being analyzed, and will be published later. Our experiment is outlined in Sec. II. Reconstruction and isolation of clean samples of the above reactions was a difficult experimental procedure, which is described in detail in Sec. III. The remaining sections present the results of the analysis. The cross sections are discussed in Sec. IV, our measurement of weak decay parameters for the  $\Xi^-$  in Sec. V, and the results of a search for strange baryons in Sec. VI.

### II. DESCRIPTION OF THE EXPERIMENT

The experiment was performed in an 11-GeV/c rf-separated  $K^-$  beam directed at the LASS spectrometer<sup>14</sup> at SLAC. Details of the experiment have been given elsewhere,<sup>15</sup> and are only briefly reiterated here. Scintillation counter hodoscopes and 10 planes of proportional wire chambers with 1-mm wire spacing were located in the beam to measure the momentum and trajectory of the incident kaon.

The LASS spectrometer is shown schematically in Fig. 1. It consists of a large superconducting solenoid vertex detector followed by a dipole spectrometer. The 23-kG solenoid field is parallel to the horizontal beam direction while the dipole field has a dominant vertical component with a field integral of 30 kG m along the beam axis. In-

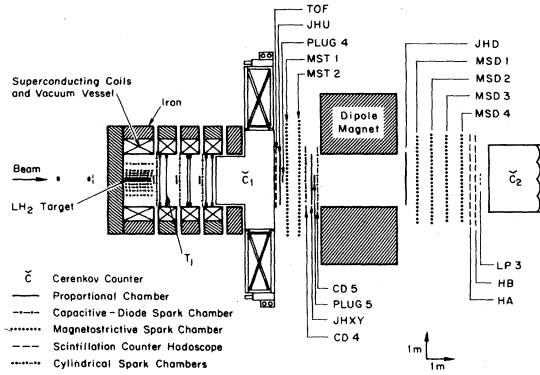


FIG. 1. Plan view of the LASS spectrometer.

teraction products which have momenta  $\lesssim 3 \text{ GeV}/c$  and which are not produced too close to the beam axis are effectively measured by the solenoid while particles with momenta  $\geq 1.5 \text{ GeV}/c$  close to the beam line are momentum analyzed in the dipole spectrometer.

The 91.6-cm-long liquid- $\text{H}_2$  target was situated on the axis of the solenoid and was surrounded by an inner cylindrical proportional wire chamber (PWC) and five outer cylindrical capacitive-diode (CD) readout spark chambers arranged coaxially, each having two spark gaps and providing three coordinate measurements. The region downstream of the target was instrumented with planar CD chambers, PWC planes, and three segmented cathode readout foil chambers. The spark gaps were deadened in the high-flux region around the solenoid axis because of their relatively long memory time. These deadened regions were overlapped by PWC's with 1-mm wire spacing and  $26 \times 26$ -cm active areas.

The dipole spectrometer, located downstream of the solenoid, consisted of a set of eight PWC planes, two CD spark chambers, and two magnetostrictive (MS) readout spark chambers upstream from the dipole electromagnet,

and four MS chambers, one PWC plane, and two segmented scintillator hodoscopes downstream of the dipole. Each MS chamber had two spark gaps and provided four coordinate measurements. Particle identification was provided by a large threshold-Cerenkov counter ( $C_1$ ) which filled the downstream aperture of the solenoid; a 24-segment circular time-of-flight (TOF) array in the solenoid, and by a large, threshold-Cerenkov counter ( $C_2$ ) downstream.

The very loose trigger, which essentially required two or more charged particles to emerge from the target, had almost complete acceptance for the events of interest here. An event was recorded if it had (1) a well-measured incident kaon, (2) no particle remaining in the beam at the end of the spectrometer, (3) two or more hits outside a 3.2-cm-square beam hole in the full aperture proportional chamber ( $T_1$  in Fig. 1) located 54 cm downstream of the target, and, (4) at least one TOF hit. Additional triggers were mixed with the event trigger to provide a sample of events to study the spectrometer performance.

### III. SAMPLE SELECTION

#### A. Preliminary extraction

Isolation of our  $\Xi^-$  and  $\Omega^-$  data samples is summarized in Tables I and II, respectively, and described below. A total of  $40 \times 10^6$  triggers were recorded on tape. All events were processed through a preliminary analysis program whose major functions included track finding (grouping of the various coordinate readouts into tracks), track fitting (assigning momenta, etc.), beam track reconstruction, and topology testing. Primary output from this program for each event then included a list of tracks with estimates of their momenta, and possible topological assignments relating tracks to production and decay vertices. The topology of interest to this study is illustrated in Fig. 2. We also reconstructed events having an additional, visible  $K^0$  decay. The  $p$  and  $\pi$  from the  $\Lambda$  decay

TABLE I. Selection criteria for  $V^-$  candidates.

	Total events left	Signal/background <sup>a</sup> in $\Xi^-$ range $1310 \leq M_{\Lambda\pi^-} \leq 1332 \text{ MeV}/c^2$
Total triggers in experiment	$40 \times 10^6$	
Primary analysis indicates $V^-$ topology is possible	405 000	21 002/29 773
Multivertex fit with confidence level $\geq 10^{-6}$	184 960	17 942/13 786
$1.2 \leq M_{\Lambda\pi^-} \leq 1.4 \text{ GeV}$ ( $\Xi^-$ )		
$1.6 \leq M_{\Lambda\pi^-} \leq 1.8 \text{ GeV}$ ( $\Omega^-$ )	109 940	17 942/13 786
Vertices correctly ordered after fitting	81 993	17 767/10 735
Vertices within fiducial volume	77 959	16 387/9 669
All tracks in time where determined	77 905	16 380/9 647
All tracks consistent with particle identification	67 997	15 859/7 825
$\Xi^-$ (or $\Omega^-$ ) production kinematically possible	55 200 ( $\Omega$ )	
Length of $V^- > 5 \text{ cm}$	65 213	15 573/7 292
	52 852 ( $\Omega$ )	
	22 841	12 553/963
	2 304 ( $\Omega$ )	

<sup>a</sup>Estimated from fits to mass distributions.

TABLE II. Additional  $\Omega^-$  event criteria.

Requirement	Number remaining	Signal/background <sup>a</sup> $1.657 \leq M_{\Lambda K} \leq 1.687$
Length of $V^- > 5$ cm and $> 4\sigma$	2304	
Event is not $\Xi^-$	1758	
Confidence levels for both geometrical and $\Lambda$ mass constrained fits $\geq 2\%$	882	
Cosine helicity $> 0.475$	579	125/115
$\Omega^- < 3.5$ decay lengths	501	96/80

were required to have an effective mass  $1.10 \leq M_{p\pi^-} \leq 1.13$   $\text{GeV}/c^2$  at their point of closest approach and to point back to a negative track giving a  $\Lambda\pi^-$  effective mass in the range  $1.2-1.4$   $\text{GeV}/c^2$  for a  $\Xi^-$  candidate, or a  $\Lambda K^-$  mass between  $1.6$  and  $1.8$   $\text{GeV}/c^2$  for an  $\Omega^-$  candidate. The lengths of the reconstructed  $\Lambda$ ,  $K^0$  and  $\Xi^-$  (or  $\Omega^-$ ) connecting tracks were required to be at least 2 cm. The  $V^-$  candidate track is typically rather short and, indeed,  $\Xi^-$  and  $\Omega^-$  particles have lifetimes such that they usually decay within the target volume. However, to reduce the large background from events with no real  $\Xi^-$  or  $\Omega^-$ , the  $V^-$  connecting length was also required to be 2 cm. These loose criteria defined 405 000 preliminary candidates for the  $\Xi^-$  and  $\Omega^-$  topologies which were extracted for further study.

After these requirements, the  $\Lambda\pi^-$  effective-mass distribution, shown in Fig. 3, showed a clear  $\Xi^-$  signal. A fit to this mass plot<sup>16</sup> gave an estimated  $\Xi^-$  signal of  $21\,000 \pm 250$  above 30 000 background. However, because of the large remaining background, there was very little clearly observed  $\Omega^-$  in the corresponding  $\Lambda K^-$  mass spectrum.

### B. Geometric constraints

The considerable backgrounds in these distributions resulted, primarily, from the fake  $V^-$ 's produced by combining  $\Lambda$ 's with the large number of negative tracks available at the primary vertex. This problem was made more difficult because the spark-chamber resolution was typically about 1 mm, and tracks near the vertices were often overlapped. In an attempt to improve the vertex resolution and hence to allow a cleaner  $V^-$  selection, all events from the samples described above were subjected to two multivertex fits, using all measured coordinates. The first

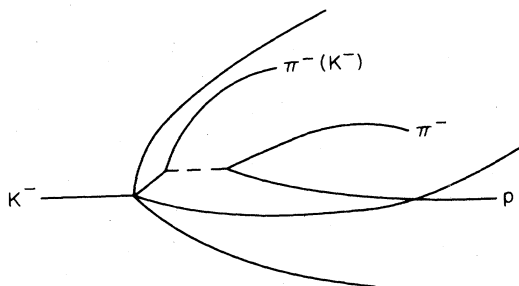


FIG. 2. The  $V^-$  topology. Selected events included all possible charge multiplicities and the possible existence of  $K^0 \rightarrow \pi^+\pi^-$  decays in addition to the topology shown.

constrained all tracks from a common vertex to emerge from a single point, and required the reconstructed  $\Lambda$ ,  $K^0$  or  $\Xi^-$  ( $\Omega^-$ ) tracks to have three-momenta such as to correctly connect their beginning and ending vertices. In the second of these fits, the effective mass of the  $V^0$  from the kink was constrained to be that of the  $\Lambda$ . Only events in which at least one of these fits was obtained with a confidence level greater than  $10^{-6}$  and vertices correctly ordered and in acceptable fiducial volumes were considered further.

### C. Particle-identification cuts

Another major source of background arose from  $\gamma \rightarrow e^+e^-$  or  $K^0 \rightarrow \pi^+\pi^-$  mistakenly identified as  $\Lambda$ 's. Many such cases were removed with the help of the particle-identification devices. For instance, events with a proton (from an assumed  $\Lambda$  decay) or  $K^-$  (from an assumed  $\Omega^-$  decay) producing light in  $C_1$  or  $C_2$ , or having times of flight more than six standard deviations from

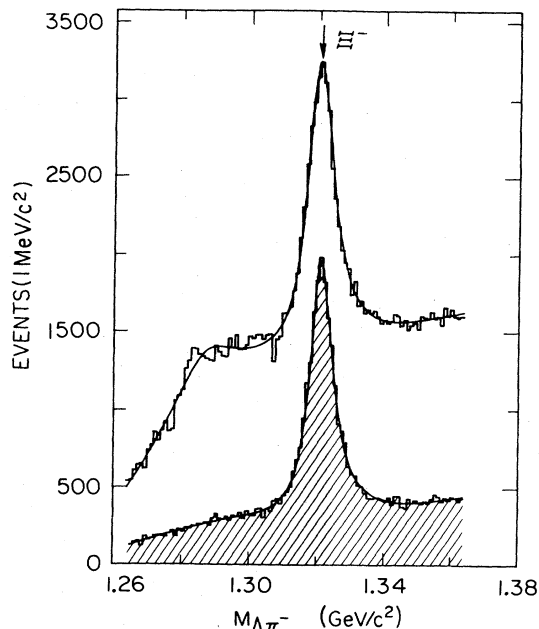


FIG. 3. Effective-mass distribution of the  $\Lambda\pi^-$  system. The unshaded distribution corresponds to all candidates for the  $V^-$  topology. The shaded plot contains only those events that make multivertex, geometrically constrained fits, and have satisfactory particle identifications as described in the text. The curves result from a fit described in the text (Ref. 16).

those expected, were rejected. Likewise, events with identified protons from the production vertex were removed. Conversions of  $\gamma \rightarrow e^+e^-$  were readily identified by the fact that, for such events interpreted as  $\Lambda \rightarrow \pi^- p$  the cosine of the angle between  $p$  and  $\Lambda$  in the  $\Lambda$  rest frame peaked sharply at values above 0.97.

#### D. Final samples

After these cuts the  $\Xi^-$  signal ( $15\,570 \pm 150$  events above 7300 background) was very clear in the  $\Lambda\pi^-$  mass plot (shaded in Fig. 3). Our final  $\Xi^-$  sample shown in Fig. 4 resulted from requiring a  $\Xi^-$  track length of at least 5 cm. The fit shown indicated that the peak contained  $12\,550 \pm 130$  events above 960 background,<sup>16</sup> and that the  $\Xi^-$  mass (with resolution of  $3 \text{ MeV}/c^2$ ) was  $1321.4 \pm 0.1 \text{ MeV}/c^2$ , in excellent agreement with the World average.<sup>17</sup>

Because of the much smaller  $\Omega^-$  production cross section, more stringent geometric requirements were enforced to further reduce the background. Figure 5 shows the  $\Lambda K^-$  mass distribution when the  $V^-$  fitted track length was at least 2 cm, when  $\Xi^-$  candidates were removed, and when both multivertex fits were required to have a confidence level greater than 2%. The signal contained  $143 \pm 25$  events, with a background of about 420 events. To obtain our final  $\Omega^-$  sample, two further selections were made. First, we required the  $V^-$  decay length to be greater than 5 cm and less than  $3.5 \Omega^-$  lifetimes. We also required that the  $V^-$  decay point be removed by at least four standard deviations from the primary vertex.

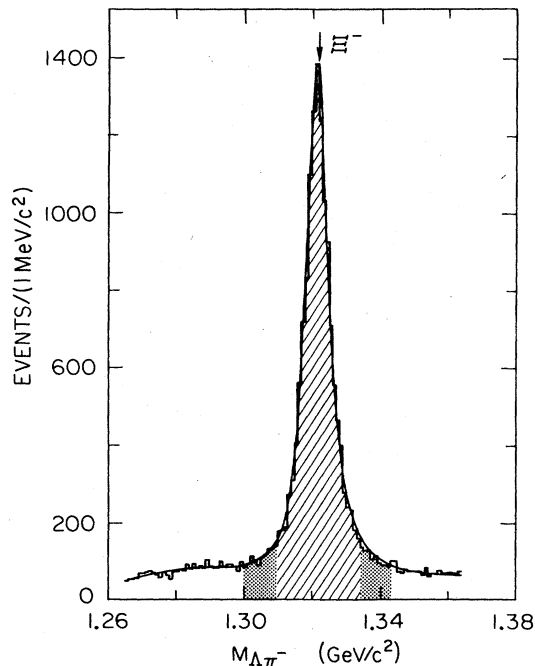


FIG. 4. Final  $\Xi^-$  sample. The  $\Lambda\pi^-$  effective-mass distribution contains only events after final cuts as described in the text. The line-shaded events clearly contain some background whose effect is monitored by the dotted events in the control regions on either side.

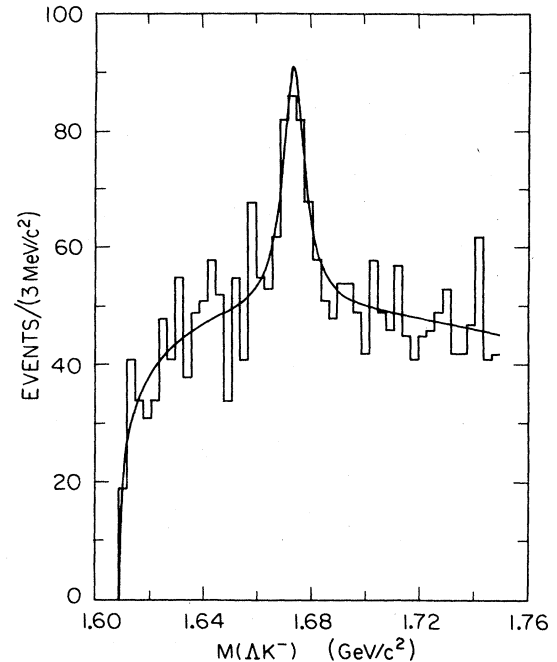


FIG. 5.  $\Lambda K^-$  effective mass. Events plotted have confidence levels  $>2\%$  for both multivertex fits, and a fitted  $V^-$  track length of at least 2 cm. Events with  $M_{\Lambda\pi^-}$  within  $11 \text{ MeV}/c^2$  of  $\Xi^-$  have been removed.

Second, events for which  $\cos\theta$ —the cosine of the angle between  $\Lambda$  and  $(\Lambda K^-)$  in the  $(\Lambda K^-)$  rest frame—was greater than  $+0.475$  were removed. This cut removed both the fake background events with small  $\Lambda K^-$  labora-

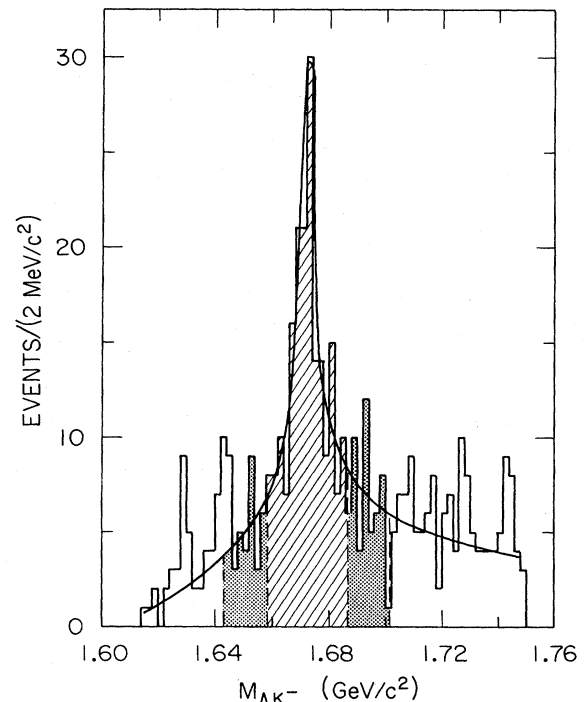


FIG. 6. Final  $\Omega^-$  sample. Line-shaded and dotted events indicate the signal and sideband subtraction regions, respectively. The curve comes from a fit described in the text (Ref. 16).

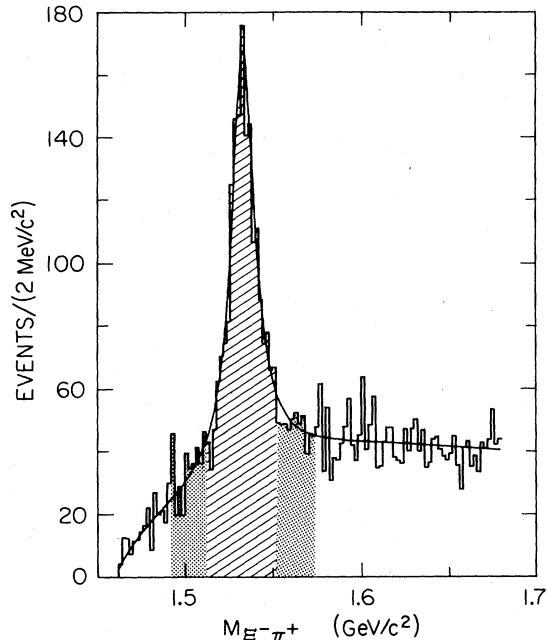


FIG. 7.  $\Xi^- \pi^+$  effective-mass distribution. Line-shaded and dotted events indicate signal and sideband subtraction regions, respectively. The curve comes from a fit described in the text (Ref. 16).

tory opening angle where the  $V^-$  track length was poorly measured as well as the remaining  $\Xi^-$  signal in an unbiased way. The final sample shown in Fig. 6 contained  $96 \pm 15 \Omega^-$  events above 80 background. The fitted  $\Lambda K^-$  mass resolution was  $4 \text{ MeV}/c^2$ , and the  $\Omega^-$  mass was  $1672.2 \pm 0.2 \text{ MeV}/c^2$ , in agreement with the world average.<sup>17</sup>

#### E. Background subtraction

All the following plots use background-subtracted data samples. In defining these samples, events were chosen which lay within  $\pm 22 \text{ MeV}/c^2$  of the  $\Xi^-$  ( $\pm 30 \text{ MeV}/c^2$  of the  $\Omega^-$ ) in  $\Lambda \pi^-$  ( $\Lambda K^-$ ) effective mass. Those events outside  $\pm 11 \text{ MeV}/c^2$  for the  $\Xi^-$  or  $\pm 15 \text{ MeV}/c^2$  for the  $\Omega^-$  were weighted negatively so as to subtract the effects of background under the respective peaks. These subsamples of signal and control band events are, respectively, the line-shaded and dotted regions in Figs. 4 and 6. The distribution of  $(\Xi^- \pi^+)$  effective-mass combinations made in this way is shown in Fig. 7 in the low-mass region. A clear  $\Xi^0$  (1530) signal is seen which has a fitted mass and width (not correcting for the resolution of  $6 \text{ MeV}/c^2$ ) of  $1532.1 \pm 0.4$  and  $17 \pm 1 \text{ MeV}/c^2$ , respectively. It contains  $1244 \pm 50$  events above background. Our  $\Xi^0$  (1530) sample was chosen from a mass band  $\pm 40 \text{ MeV}/c^2$  from  $1532 \text{ MeV}/c^2$ , where events outside the  $\pm 20\text{-MeV}/c^2$  range were used for purposes of background subtraction.

### IV. CROSS SECTIONS

#### A. Monte Carlo simulation

In order to compute the total acceptance of the spectrometer, including the reconstruction program and the

above selection criteria, a large number of events corresponding to  $\Xi^-$ ,  $\Omega^-$ , and  $\Xi^0$  (1530) production were generated (the "thrown" Monte Carlo sample), and subjected to a computer simulation of conditions in the experiment and hardware including software requirements. Those surviving (the "passing" Monte Carlo sample) were an indication of the overall acceptance for production and decay of these particles. In this process, for example, "raw" data similar to that from a real  $\Xi^-$  event would be simulated by computer propagation of all associated particles, from their appropriate vertices, through the known magnetic field and geometric arrangement of detectors in the LASS spectrometer. A fake set of coordinates in the tracking chambers, and analog-to-digital-converter (ADC) and time-to-digital-converter (TDC) readings in the scintillation and Cerenkov chambers, etc., were thus produced. The resulting set of coordinates, etc., were then processed through the same programs and selections as the actual data. Some effects taken into consideration in this simulation included multiple scattering, absorption, resolution of various detectors, energy loss, and weak decay probabilities.

#### 1. Monte Carlo distributions

The thrown sample needed to simulate (a) the primary vertex location in the target, (b) the beam momentum vector, (c) the rotation of the event about the beam axis, (d) the lifetime distributions of decaying particles ( $\Omega^-$ ,  $\Xi^-$ ,  $\Lambda$ ,  $K^0$ ), (e) the decay distributions of these particles, and (f) the hyperon production characteristics.

Items (a)–(d) were readily simulated, using well-known properties of the beam and lifetimes for the particles.<sup>17</sup> Hyperon decays—item (e)—were generated isotopically in the parent rest frames. Other distributions were found to make rather little difference to the overall acceptance. To simulate the hyperon production characteristics, item (f), we used the four-momenta for production particles from events in the data samples themselves. In this way, effects of correlations between these particles, as well as their momentum distributions, were, at least partially, taken into account in our Monte Carlo sample.

#### 2. Efficiencies

Approximately 40 randomized variations of each data sample event were generated and processed through the spectrometer, as described. The resulting efficiency  $\epsilon$  (= number passing/number thrown) was found to depend significantly upon three variables defined as  $x$  [(hyperon momentum in c.m. system)/(maximum possible value) =  $p_L/p_{\text{max}}$ ],  $p_T^2$  (square of hyperon transverse momentum),  $n$  (number of primary charged particles).

Figures 8(a) and 8(b) show the efficiencies as functions of  $x$  and  $p_T^2$  for the three hyperons being considered here. They are characterized by a significant drop in efficiency at  $x < -0.5$  due to low-momentum hyperons failing to travel far enough before decaying, and at  $x > 0.8$  due to  $\Lambda$  decays occurring beyond the decay fiducial volume defined by the detectors. Variations of  $\epsilon$  with  $p_T^2$  were much less dramatic, falling slightly with increasing values. The relative efficiencies for primary charged par-

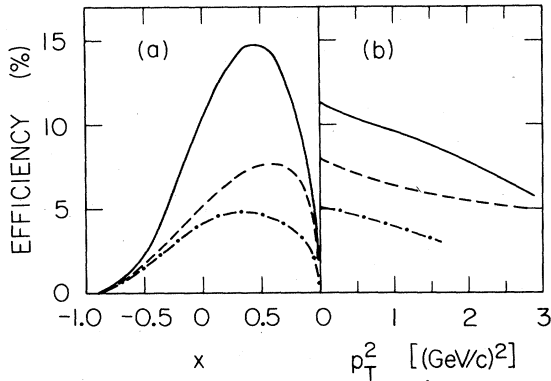


FIG. 8.  $\Xi^-$ ,  $\Omega^-$  and  $\Xi^0(1530)$  acceptances. (a) The acceptance for each hyperon, as a function of  $x$ , integrated over  $p_T^2$ ; (b) acceptance versus  $p_T^2$  integrated over  $x$ . The solid curves are for  $\Xi^-$ ; the dashed curves for  $\Xi^0(1530)$  and the dot-dashed curves for  $\Omega^-$ .

ticle multiplicities of 2:4:6 were approximately 100:75:50 in all cases.

Each Monte Carlo event was assigned a weight  $w$  (normalized to have mean value = 1.0) given by

$$w(x, p_T^2, n) \propto \epsilon^{-1}(x, p_T^2, n),$$

so that the distributions of  $x$ ,  $p_T^2$ , and  $n$  for passing Monte Carlo events matched those for the data sample. Various distributions of other quantities then also showed good agreement between the passing Monte Carlo events and the data—a test of the overall simulation process. For example, Fig. 9 compares the proper lifetime distribution for the  $\Xi^-$  data with the Monte Carlo prediction (solid line). Similarly, the  $\Xi^-$  production vertex position is compared in Fig. 10. The resolution of the reconstructed  $\Xi^-$  and  $\Omega^-$  masses from the Monte Carlo events also agreed within a few tenths of an  $\text{MeV}/c^2$  with those observed in the data.

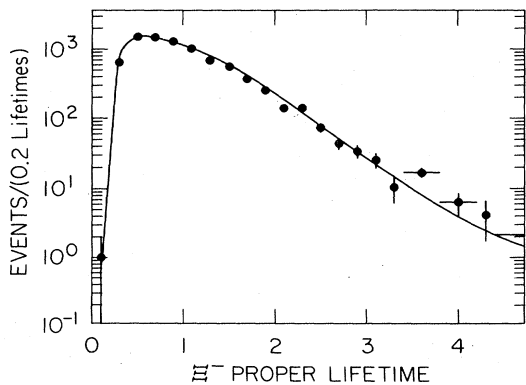


FIG. 9.  $\Xi^-$  lifetime distribution. The uncorrected lifetime distribution for  $\Xi^-$  events shows deviations from linearity due to acceptance effects. The curve represents the Monte Carlo simulation of this distribution.

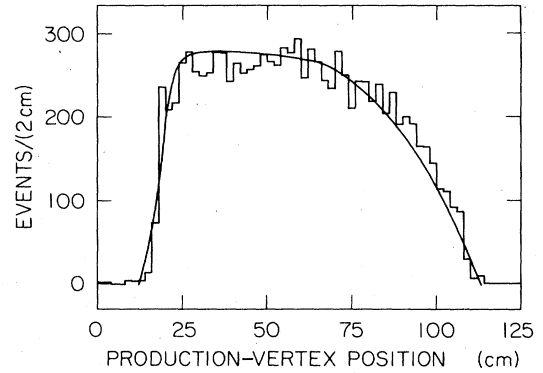


FIG. 10. Production-vertex distribution for  $\Xi^-$  events. The curve represents the Monte Carlo simulation of this distribution.

## B. Total cross sections

Total cross sections were computed from a combination of factors:

$$\sigma_{\text{tot}} = N \left[ \frac{1}{\epsilon} \right] \left[ \frac{1}{\nu} \right] \left[ \frac{1}{b} \right] \left[ \frac{1}{1427} \right]$$

in which  $\nu$  was the branching ratio for  $\Lambda \rightarrow p\pi^-$ ,  $N$  the number of events in the data above background,  $\epsilon$  ( $= \sum_{\text{passing}} w / \sum_{\text{thrown}} w$ ) the average efficiency, and  $b$  the branching ratio for the observed  $V^-$  decay mode. The values used were  $b(\Xi^- \rightarrow \Lambda\pi^-) = 1.0$ ,  $b(\Xi^0(1530) \rightarrow \pi^+\Xi^-) = \frac{2}{3}$ ,  $b(\Omega^- \rightarrow \Lambda K^-) = 0.686$ , and  $\nu(\Lambda \rightarrow p\pi^-) = 0.642$ . The overall normalization was 1427 events/ $\mu\text{b}$ .

Cross sections were also computed as a function of production multiplicity in a similar way using, in the above relationship, the multiplicity-dependent efficiencies  $\epsilon(n)$  rather than  $\epsilon$ . The results for  $\Xi^-$ ,  $\Xi^0(1530)$ , and  $\Omega^-$  are given in Table III and plotted as functions of  $K^-$  momentum in Figs. 11(a), 11(b), and 11(c) for comparison with other available data. Agreement amongst experiments is generally good. The  $\Xi^-$  total cross section is almost independent of beam momentum, while the higher-multiplicity cross sections rise sharply. The  $\Omega^-$  and  $\Xi^0(1530)$  total cross sections also appear to show little beam-momentum dependence near 11  $\text{GeV}/c$ .

## C. Inclusive production characteristics

### 1. Particle multiplicities

The average number of charged tracks  $\langle n \rangle$  at the production vertex is summarized in Table III for the data samples reported to date. At a given  $s$ , values for this quantity show a clear tendency to smaller values for the higher-hyperon masses. Figure 12 shows  $\langle n \rangle$  as a function of  $\ln(s)$ . There is sufficient data so that a meaningful energy dependence can only be established for the  $\Xi^-$  where a simple linear fit in  $\ln(s)$  gives a variation of the form  $\langle n \rangle \sim s^{0.46 \pm 0.03}$ .

TABLE III. Hyperon inclusive production characteristics (cross sections in  $\mu\text{b}$ ).

Reaction	$K^-$ momentum (GeV/c)	Approx. No. of events	$\sigma_{\text{tot}}$	2 prong	4 prong	6 prong	8 prong	$\langle n_{\text{ch}} \rangle$	$\langle x \rangle$	$\langle p_T \rangle$ (GeV/c)	$B$ [(GeV/c) $^{-2}$ ]
$K^- p \rightarrow \Xi^- + X$	11 <sup>a</sup>	12553	133 $\pm$ 15	25 $\pm$ 6	76 $\pm$ 11	29 $\pm$ 7	4 $\pm$ 3	3.9 $\pm$ 0.2	0.24 $\pm$ 0.01	0.502 $\pm$ 0.005	3.14 $\pm$ 0.06
	4.2 (Ref. 1)	5046	157 $\pm$ 8	106.6 $\pm$ 5.6	49.6 $\pm$ 2.8	0.7 $\pm$ 0.2		2.65 $\pm$ 0.05	0.24 $\pm$ 0.01	0.448 $\pm$ 0.003	3.9 $\pm$ 0.01
	6.5 (Ref. 4)	440	160 $\pm$ 8								
	8.25 (Ref. 2)	8121	157 $\pm$ 10	47.5 $\pm$ 3	90.4 $\pm$ 5.8	18.8 $\pm$ 1.2	0.3 $\pm$ 0.1	3.64 $\pm$ 0.04	0.24 $\pm$ 0.01	0.512 $\pm$ 0.003	3.09 $\pm$ 0.33
	10 (Ref. 3)	876	172 $\pm$ 20	38 $\pm$ 9	101 $\pm$ 15	31 $\pm$ 8	2 $\pm$ 2	4.0 $\pm$ 0.01	0.23 $\pm$ 0.04	0.52 $\pm$ 0.01	3.1 $\pm$ 0.2
	14.3 (Ref. 5)		127 $\pm$ 9	14 $\pm$ 2	63 $\pm$ 6	44 $\pm$ 6	6 $\pm$ 3	4.7 $\pm$ 0.2	0.16 $\pm$ 0.05	0.44 $\pm$ 0.04	
16 (Ref. 3)	861	135 $\pm$ 15	18 $\pm$ 5	61 $\pm$ 9	47 $\pm$ 3	9 $\pm$ 4	4.7 $\pm$ 0.01	0.22 $\pm$ 0.02	0.59 $\pm$ 0.01	2.6 $\pm$ 0.1	
$K^- p \rightarrow \Xi^0(1530) + X$	11 <sup>a</sup>	1244	44 $\pm$ 6	5 $\pm$ 2	22 $\pm$ 4	17 $\pm$ 4	1 $\pm$ 1	4.1 $\pm$ 0.2	0.09 $\pm$ 0.02	0.55 $\pm$ 0.03	2.6 $\pm$ 0.2
	4.2 (Ref. 1)		30 $\pm$ 3						0.09 $\pm$ 0.01		
	6.5 (Ref. 4)		38 $\pm$ 3								
	8.25 (Ref. 2)	2 772	45 $\pm$ 3						0.16 $\pm$ 0.03	0.51 $\pm$ 0.02	2.59 $\pm$ 0.06
	10 (Ref. 3)		43 $\pm$ 7	3 $\pm$ 3	23 $\pm$ 5	1 $\pm$ 1			0.13 $\pm$ 0.05	0.55 $\pm$ 0.02	2.8 $\pm$ 0.4
	16 (Ref. 3)		32 $\pm$ 5	1 $\pm$ 1	18 $\pm$ 4	11 $\pm$ 3	2 $\pm$ 1		0.10 $\pm$ 0.05	0.63 $\pm$ 0.02	2.0 $\pm$ 0.3
$K^- p \rightarrow \Omega^- + X$	11 <sup>a</sup>	96	3.9 $\pm$ 0.6	1.2 $\pm$ 0.3	2.7 $\pm$ 0.5	0.03 $\pm$ 0.03	<0.03	3.2 $\pm$ 0.3	0.11 $\pm$ 0.04	0.57 $\pm$ 0.05	2.3 $\pm$ 0.3
	4.2 (Ref. 1)	40	0.5 $\pm$ 0.1								
	6.5 (Ref. 4)	15	1.4 $\pm$ 0.6								
	8.25 (Ref. 2)	67	2.1 $\pm$ 0.3					2.88 $\pm$ 0.09	0.19 $\pm$ 0.02	0.56 $\pm$ 0.03	2.8 $\pm$ 0.2
	10 (Ref. 3)		3.7 $\pm$ 0.9								
	16 (Ref. 3)		3.2 $\pm$ 1.1								

<sup>a</sup>This experiment.

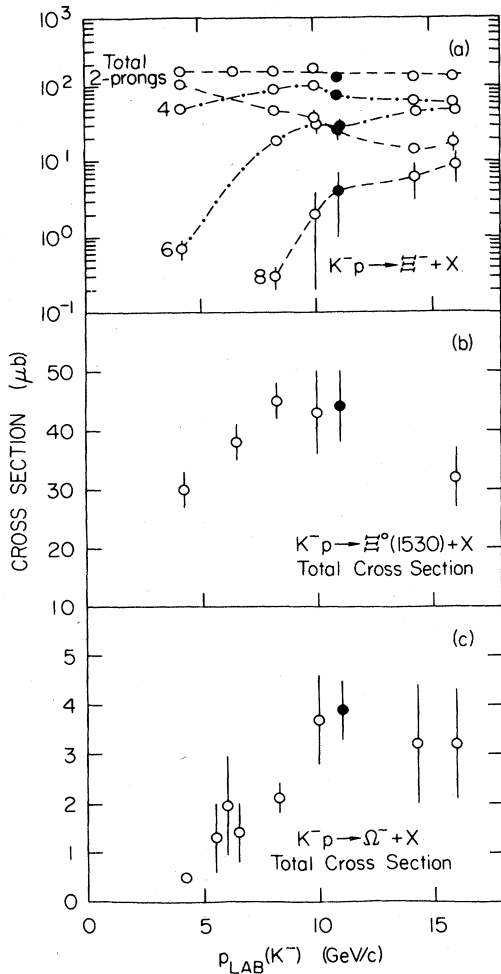


FIG. 11. Total cross sections. (a)  $K^-p \rightarrow \Xi^- + \text{anything}$ ; (b)  $K^-p \rightarrow \Xi^0(1530) + \text{anything}$ ; (c)  $K^-p \rightarrow \Omega^- + \text{anything}$ . Cross sections are shown as a function of  $K^-$  momentum in the laboratory. Where data exist, cross sections for different multiplicities are shown. The values for this experiment are indicated by the solid points. The curves are included to guide the eye only.

## 2. Longitudinal momentum

It is usual to describe inclusive momentum distributions in terms of the Feynman variable  $x = p_L/p_{\text{max}}$  and the square of the transverse momentum  $p_T^2$  already referred to in Sec. IV A 2. The invariant distribution  $F(x)$  is defined as

$$F(x) = \frac{1}{\pi p_{\text{max}}} \int E \frac{d^2\sigma}{dx dp_T^2} dp_T^2,$$

where  $p_L$  and  $p_T$  are longitudinal and transverse components of the momentum of the hyperon, respectively, in the overall center-of-mass system, while  $p_{\text{max}}$  and  $E$  are the maximum possible momentum and energy in this system.

These invariant distributions are tabulated in Table IV

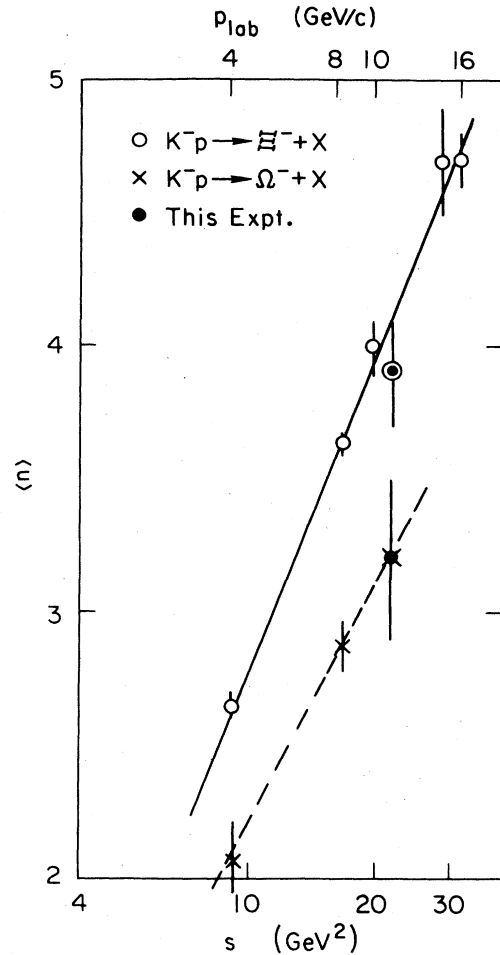


FIG. 12. Mean charged multiplicity vs  $s$  for the reactions  $K^- \rightarrow \Xi^- + \text{anything}$  and  $\Omega^- + \text{anything}$ . A fit of the  $\Xi^-$  data to the form  $\langle n \rangle \propto s^{0.46 \pm 0.03}$  is shown. The dashed line for the  $\Omega^-$  data is included only to guide the eye.

and shown for each of the three hyperons in Figs. 13(a), 14(a), and 15(a). The mean values of  $x$  from these distributions, summarized in Table III, are all positive, indicating a substantial amount of hyperon exchange contribution to the production of each of these particles. Data from other energies, where available, are included in Table III and in Figs. 13, 14, and 15. In the  $\Xi^-$  case, there is very little variation with beam energy in the values for  $\langle x \rangle$  and also very little variation in the shape of  $F(x)$  at different  $s$  values, with the possible exception of one point from the 16-GeV/c data near  $x = +1$ . In general, however, the magnitude of  $F(x)$  appears to decrease noticeably at all  $x$  values as  $s$  increases. This is slightly more noticeable at large positive  $x$  values where hyperon exchange production would be expected to dominate. Possibly, at higher  $s$ , the production of  $\Xi^-$  is more the result of  $\Xi^*$ ,  $Y^*$ , or even  $\Omega^*$  decays. Data from the  $\Omega^-$  and  $\Xi^*(1530)$  reactions have, within the statistical uncertainties presented, a behavior consistent with the  $\Xi^-$ .



TABLE IV. Invariant  $x$  distributions.

$x$ range		$K^-p \rightarrow \Xi^- + X$		$K^-p \rightarrow \Omega^- + X$		$K^-p \rightarrow \Xi^0(1530) + X$	
Low	High	Weighted No. of events	$F(x)$ ( $\mu\text{b}$ )	Weighted No. of events	$F(x)$ ( $\mu\text{b}$ )	Weighted No. of events	$F(x)$ ( $\mu\text{b}$ )
-0.95	-0.55	35	3.8±1.6	1		6	
-0.55	-0.50	22	7.5±1.8			5	
-0.50	-0.45	44	10.7±1.7	2		11	
-0.45	-0.40	59	10.4±1.5		0.4±0.3	11	1.9±0.7
-0.40	-0.35	85	12.1±1.4			0	
-0.35	-0.30	98	11.2±1.2	9		11	
-0.30	-0.25	130	12.3±1.1			23	
-0.25	-0.20	181	14.4±1.1			20	4.6±1.9
-0.20	-0.15	226	15.6±1.1			12	3.6±1.1
-0.15	-0.10	317	19.1±1.1	19	1.5±0.5	27	3.6±1.1
-0.10	-0.05	367	19.6±1.1			40	6.6±2.2
-0.05	0	449	21.9±1.1			37	5.6±1.9
0	0.05	529	24.0±1.1			41	5.9±2.0
0.05	0.10	565	24.0±1.1	17	1.0±0.4	63	8.3±2.4
0.10	0.15	679	27.4±1.1			69	8.8±1.5
0.15	0.20	727	28.3±1.1			76	9.4±1.6
0.20	0.25	785	29.8±1.1			67	7.9±1.6
0.25	0.30	809	30.3±1.1			61	7.1±1.4
0.30	0.35	802	30.2±1.1	17	0.9±0.3	96	11.0±1.6
0.35	0.40	800	30.6±1.1			94	10.7±1.6
0.40	0.45	703	27.5±1.1			56	6.5±1.5
0.45	0.50	720	29.2±1.1			82	9.4±1.5
0.50	0.55	665	28.2±1.1	22	1.3±0.3	59	6.9±1.4
0.55	0.60	567	25.5±1.1			55	6.6±1.5
0.60	0.65	505	24.5±1.1			36	4.4±1.3
0.65	0.70	449	23.7±1.2	8		40	5.2±1.2
0.70	0.75	356	21.1±1.2			30	4.0±1.0
0.75	0.80	285	19.2±1.2		0.3±0.2	29	4.0±1.0
0.80	0.85	235	18.8±1.3			24	3.6±1.0
0.85	0.90	179	17.7±1.4			12	2.0±0.7
0.90	0.95	117	15.7±1.5	1		10	
0.95	1.00	52	11.0±1.6			4	1.1±0.4

### 3. Transverse momentum

Distributions of  $p_T^2$  (integrated over  $x$ ) are shown in Figs. 13(b), 14(b), and 15(b) for the three hyperons. As observed at other momenta,<sup>1-7</sup> these are well described for  $p_T^2$  values up to 1.0  $\text{GeV}/c^2$  by a distribution of the form

$$\frac{d\sigma}{dp_T^2} = A e^{-B p_T^2}$$

Values for  $B$  are summarized for each reaction in the final column of Table III for a variety of momenta, and are characterized by the fact that they show very little dependence upon beam momentum, but decrease with hyperon mass. The major exception to this would appear to be in the  $\Xi^-$  data<sup>1</sup> at 4.2  $\text{GeV}/c$ , with a value closer to 4 than to 3, except that this value was computed only for events with  $x > 0.2$ .

Our  $\Xi^-$  data, presented in Fig. 13(b), extend to values of  $p_T^2$  up to 3.0  $(\text{GeV}/c)^2$ —rather higher than those shown for any other experiments. Above 1.0  $(\text{GeV}/c)^2$

there appears to be some excess of events above the extrapolated expectation from the smaller  $p_T^2$  values.

Very little correlation exists between  $x$  and  $p_T$  for either  $\Xi^-$  or  $\Xi^0(1530)$  production as demonstrated in Fig. 16 where  $\langle p_T \rangle$  is plotted versus  $x$ . Similar correlation distributions have also been observed at 4.2  $\text{GeV}/c$  (Ref. 1), 8.25  $\text{GeV}/c$  (Ref. 2), 10  $\text{GeV}/c$ , and 16  $\text{GeV}/c$  (Ref. 3). They are characterized by an indication of a drop in the value of  $\langle p_T \rangle$  for  $x$  near  $\pm 1$  as might be expected kinematically, but are generally rather flat.

### V. POLARIZATION AND WEAK DECAY PARAMETERS OF $\Xi^-$

Nonleptonic weak decays of hyperons are usually described by asymmetry parameters  $\alpha, \beta, \gamma$  given in terms of isospin-changing, opposite-parity, partial-wave amplitudes  $S$  and  $P$  (which corresponds to  $s$  and  $p$  wave, respectively, in  $\Xi^- \rightarrow \Lambda \pi^-$  decays).

The definitions of  $\alpha, \beta, \gamma$  are

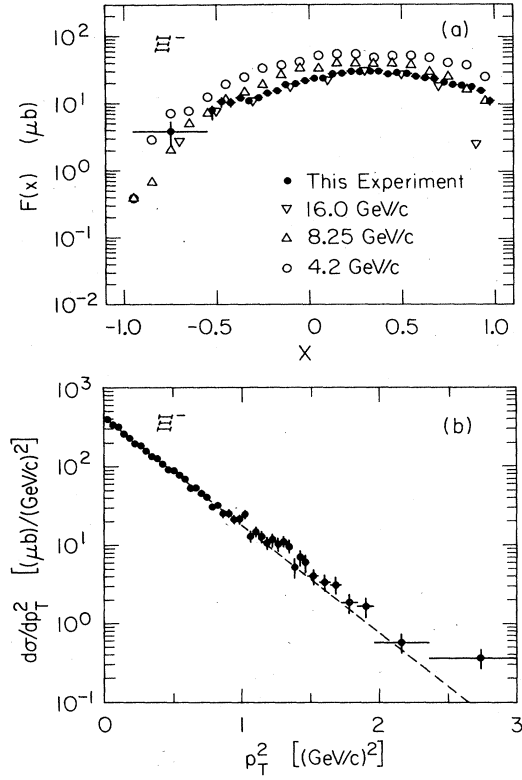


FIG. 13. Momentum distribution for  $K^-p \rightarrow \Xi^- + \text{anything}$ . (a) The invariant cross section  $F(x)$  vs  $x$  is compared with other data. To reduce confusion, error bars are included only for this experiment, whenever they are larger than the dots. Estimates of errors in all plots for this experiment include uncertainties in acceptance. Most error bars are smaller than the dots. The plots come from this experiment (12551 events), 16.0 GeV/c (933 events), 8.25 GeV/c (8121 events); 4.2 GeV/c (5046 events). (b)  $d\sigma/dp_T^2$  vs  $p_T^2$  for this experiment. The curve indicates a fit of the form  $d\sigma/dp_T^2 = (411 \pm 6) \exp(-3.14 \pm 0.06)p_T^2$ .

$$\alpha = \frac{2\text{Re}(S^*P)}{|S|^2 + |P|^2}, \quad (5.1a)$$

$$\beta = \frac{2\text{Im}(S^*P)}{|S|^2 + |P|^2} = (1 - \alpha^2)^{1/2} \sin\phi, \quad (5.1b)$$

$$\gamma = \frac{|S|^2 - |P|^2}{|S|^2 + |P|^2} = (1 - \alpha^2)^{1/2} \cos\phi, \quad (5.1c)$$

so that

$$\alpha^2 + \beta^2 + \gamma^2 = 1. \quad (5.1d)$$

In general, it is interesting to compare these parameters for different members of any given isospin multiplet as a test of the  $\Delta I = \frac{1}{2}$  rule, but the comparison of the two decays

$$\Xi^0(\Xi^-) \rightarrow \Lambda\pi^0(\pi^-)$$

is particularly interesting since the  $\Lambda\pi$  systems are purely isospin 1. This means that not only do final-state interac-

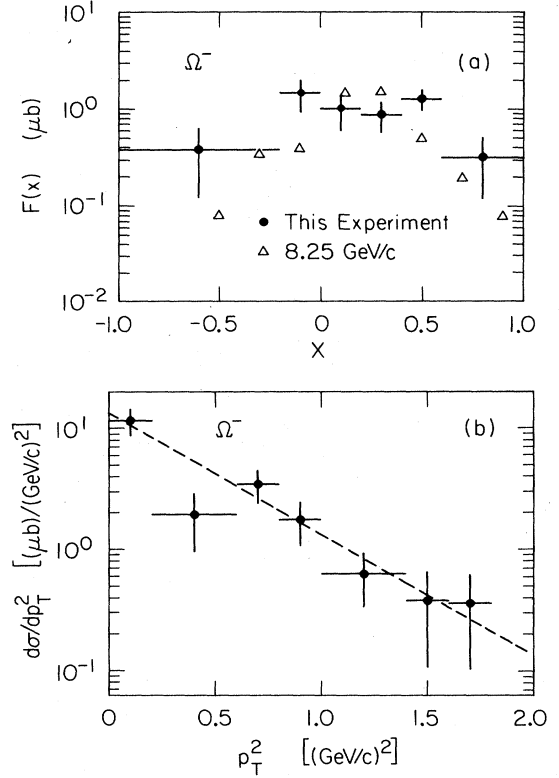


FIG. 14. Production characteristics for  $K^-p \rightarrow \Omega^- + \text{anything}$ . (a)  $F(x)$  vs  $x$ . Error bars are included only for this experiment to reduce confusion. (b)  $d\sigma/dp_T^2$  for this experiment. The fit is of the form  $d\sigma/dp_T^2 = (13 \pm 3) \exp(-2.3 \pm 0.3)p_T^2$ . Plots include 96 events from this experiment and 63 events from the 8.25-GeV/c data.

tions have similar effects in both cases, but also the isospin decay amplitudes are thereby limited to  $\Delta I = \frac{1}{2}$  or  $\frac{3}{2}$  (unlike, for example,  $\Sigma \rightarrow N\pi$  decays where final-state interactions are unknown mixtures of isospin  $\frac{1}{2}$  and  $\frac{3}{2}$  and  $\Delta I = \frac{5}{2}$  is also possible). As some discrepancy exists between recent measurements of  $\alpha_\Xi$ , it is appropriate to determine this parameter from our sample of  $\Xi^-$ .

#### A. Angular distributions

In the  $\Xi^-$  rest frame, the distribution of  $\Lambda$  momentum ( $\mathbf{\Lambda}$ ) from the decay

$$\Xi^- \rightarrow \Lambda\pi^-$$

is described in terms of the  $\Xi^-$  polarization ( $\mathbf{P}_\Xi$ ) by

$$F(\theta) = 1 + \alpha_\Xi P_\Xi \cos\theta,$$

where

$$\cos\theta = \hat{\mathbf{P}}_\Xi \cdot \hat{\mathbf{\Lambda}} \quad (\text{unit vectors}). \quad (5.2)$$

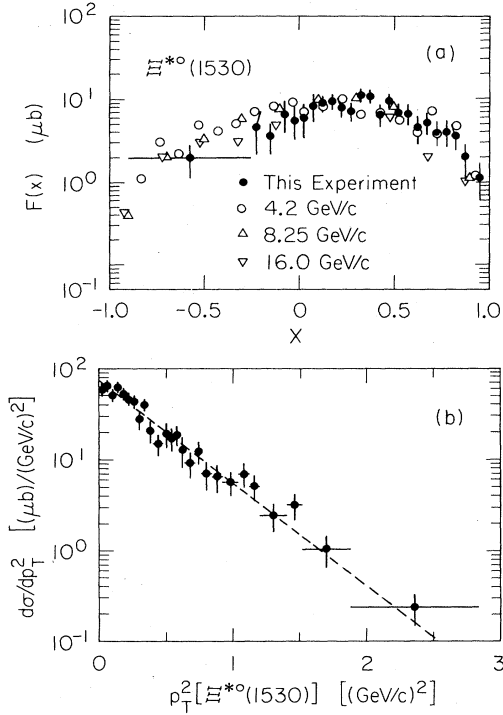


FIG. 15. Production characteristics for  $K^-p \rightarrow \Xi^*(1530) + \text{anything}$ . (a)  $F(x)$  vs  $x$ . Error bars are included only for this experiment whenever larger than the dots. (b)  $d\sigma/dp_T^2$  for this experiment. The fit is of the form  $d\sigma/dp_T^2 = (73 \pm 12) \exp(-2.6 + 0.5)p_T^2$ .

In this decay, each  $\Lambda$  acquires a polarization  $\mathbf{P}_\Lambda(\theta)$  which depends upon its emission angle  $\theta$ , and whose three components are given by<sup>18</sup>

$$\begin{aligned} P_{\Lambda_1} &= -P_\Xi \gamma_\Xi \sin\theta / F(\theta), \\ P_{\Lambda_2} &= P_\Xi \beta_\Xi \sin\theta / F(\theta), \\ P_{\Lambda_3} &= (P_\Xi \cos\theta + \alpha_\Xi) / F(\theta), \end{aligned} \quad (5.3)$$

in a coordinate system with axes  $\hat{\mathbf{e}}_1, \hat{\mathbf{e}}_2, \hat{\mathbf{e}}_3$  defined for each decay as

$$\begin{aligned} \hat{\mathbf{e}}_3 &= \hat{\Lambda}, \\ \hat{\mathbf{e}}_2 &= \frac{\hat{\mathbf{P}}_\Xi \times \hat{\Lambda}}{|\hat{\mathbf{P}}_\Xi \times \hat{\Lambda}|}, \\ \hat{\mathbf{e}}_1 &= \hat{\mathbf{e}}_2 \times \hat{\mathbf{e}}_3. \end{aligned} \quad (5.4)$$

In the subsequent decay,

$$\Lambda \rightarrow p\pi^-;$$

the direction of the proton momentum ( $\mathbf{p}$ ) in this  $\Lambda$ 's rest frame then follows the distribution

$$f(\theta, \psi) = 1 + \alpha_\Lambda P_\Lambda(\theta) \cos\psi$$

where

$$\cos\psi = \hat{\mathbf{p}} \cdot \hat{\mathbf{P}}_\Lambda(\theta). \quad (5.5)$$

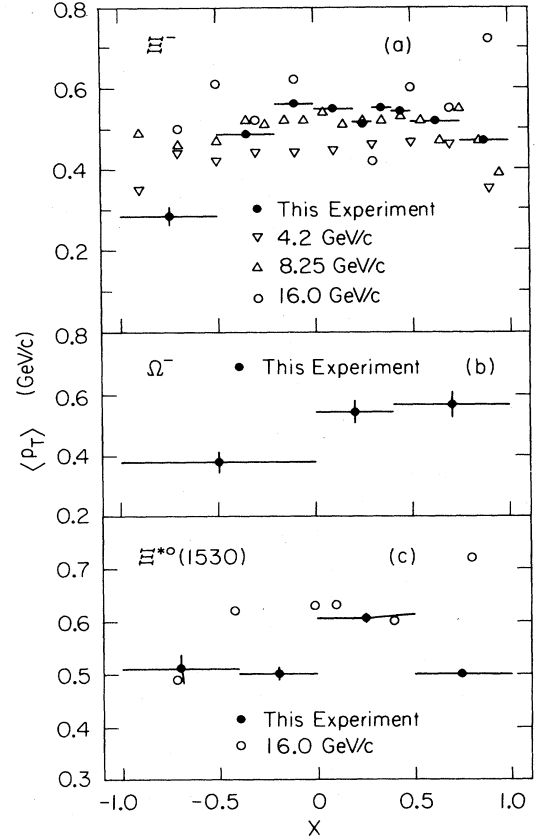


FIG. 16.  $\langle p_T \rangle$  vs  $x$ . (a)  $K^-p \rightarrow \Xi^- + \text{anything}$ ; (b)  $K^-p \rightarrow \Omega^- + \text{anything}$ ; (c)  $K^-p \rightarrow \Xi^*(1530) + \text{anything}$ . When available, other published data are included for comparison. Error bars are included only for this experiment where they are larger than the dots.

A convenient way to present the data is to show distributions of  $\cos\theta$  and of the three proton direction cosines  $\cos\psi_k = \hat{\mathbf{p}} \cdot \hat{\mathbf{e}}_k$  ( $k=1,3$ ). These are shown in Figs. 17(a)–17(d) for our entire  $\Xi^-$  sample integrated over all

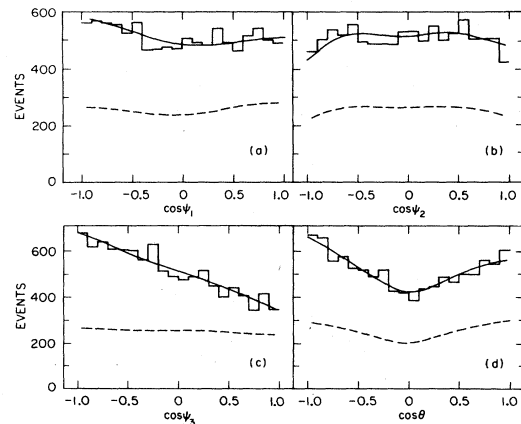


FIG. 17.  $\Xi^-$  decay angles. Distribution of the four angles  $\psi_{1-3}$  and  $\theta$  defined in the text are shown in (a)–(d), respectively. The solid curves are the result of the "x-fit" described in the text. Dotted curves indicate acceptances in these angles (in arbitrary units).

$(x, p_T^2)$  values, with their acceptances indicated by the broken curves. These acceptances are very well determined from over 30 000 passing Monte Carlo events, and show only slight variations, exhibiting no sharp dips or gaps. This is a consequence of the solenoidal symmetry of the LASS spectrometer, and is the reason we are able to make accurate determinations of  $\alpha_{\Xi}$  and also to measure the  $\Phi_{\Xi}$  parameter free from significant systematic biases. In particular, the distribution in the variable  $\cos\psi_3$ —which is usually used to determine  $\alpha_{\Xi}$ , since its slope should be equal to  $\alpha_{\Xi}\alpha_{\Lambda}$  independent of  $\Xi$  polarization—has an acceptance that varies almost linearly, with a slope which is less than 15% of  $\alpha_{\Xi}\alpha_{\Lambda}$  and is known to better than 1%.

Each distribution in Fig. 17 is expected to exhibit a linear form (after correction for acceptance). Their forms

are given by (5.2)

$$F(\theta) = 1 + \alpha_{\Xi} P_{\Xi} \cos\theta$$

and

$$f_1(\psi_1) = 1 + \frac{\pi}{4} P_{\Xi} \gamma_{\Xi} \alpha_{\Lambda} \cos\psi_1,$$

$$f_2(\psi_2) = 1 + \frac{\pi}{4} P_{\Xi} \beta_{\Xi} \alpha_{\Lambda} \cos\psi_2, \quad (5.6)$$

$$f_3(\psi_3) = 1 + \alpha_{\Lambda} \alpha_{\Xi} \cos\psi_3.$$

In addition to measuring  $\alpha_{\Xi}$ ,  $\beta_{\Xi}$ , and  $\gamma_{\Xi}$ , therefore, a determination of the slopes of these distributions could be used to measure  $P_{\Xi}$  and, in view of the constraint (5.1d), could even measure  $\alpha_{\Lambda}$ . In our fits, however, we used the value  $\alpha_{\Lambda} = 0.642 \pm 0.013$  quoted in Ref. 17.

### B. Maximum-likelihood fit

Obviously, a fit to the distributions in  $\cos\theta$  and  $\cos\psi_{1-3}$  (after acceptance correction) to the forms (5.2) and (5.6) subject to the constraint (5.1d) would provide a determination of  $\alpha$ ,  $\beta$ ,  $\gamma$ , and  $P$  for the  $\Xi^-$ . To allow for the correlations in acceptance between the various angles, however, we used a likelihood method which we describe below.

The probability for a given  $\Xi^-$  event to decay after a proper time  $t_i$  with  $\Lambda$  momentum  $\Lambda_i$  in the  $\Xi^-$  rest frame and proton momentum  $\mathbf{p}_i$  in the  $\Lambda$  rest frame is proportional to the product of the distributions (5.2) and (5.5) and an exponential decay factor that depends on the  $\Xi$  lifetime  $\tau$ :

$$\begin{aligned} W_i(\alpha_{\Xi}, \beta_{\Xi}, \gamma_{\Xi}, P_{\Xi}; \mathbf{p}_i, \Lambda_i, t_i) &= F(\theta_i) f(\theta_i, \psi_i) \exp(-t_i/\tau) \\ &= [1 + \alpha_{\Lambda} \alpha_{\Xi} \cos\psi_3 + \alpha_{\Xi} P_{\Xi} \cos\theta + \alpha_{\Lambda} P_{\Xi} (-\gamma_{\Xi} \cos\psi_1 \sin\theta + \beta_{\Xi} \cos\psi_2 \sin\theta + \cos\psi_3 \cos\theta)] \exp(-t_i/\tau). \end{aligned} \quad (5.7)$$

Clearly,  $W$  is a function of  $\Xi^-$  decay parameters and polarization, the  $\Xi^-$  lifetime  $\tau$  and  $\alpha_{\Lambda}$ . Less obviously, it is also a function of the magnetic moment  $\mu_{\Xi}$  of the  $\Xi^-$ , since the polarization of each event precesses from its original direction parallel to  $(\mathbf{K}_{\text{beam}} \times \Xi^-)$  by an amount proportional to  $\mu_{\Xi} t_i$  before decay. In principle, therefore, this method could be used to determine all these quantities, though we found that, in practice, our data were rather insensitive to  $\mu_{\Xi}$ .

Each event occupied a point in phase space (denoted here by a set of kinematic variables  $\omega_i$ ) and had an unknown acceptance  $A_i(\omega_i)$  and a production distribution  $B(\omega_i)$  both of which depended, in general, upon all of the  $\omega_i$ . The likelihood function for the ensemble of  $N$  events in our own sample, therefore, was

$$L = \prod_{i=1}^N A_i(\omega_i) B_i(\omega_i) W_i(\alpha_{\Xi}, \beta_{\Xi}, \gamma_{\Xi}, P_{\Xi}; \omega_i). \quad (5.8)$$

In the formulation of the extended log-likelihood method,<sup>19</sup> therefore, it was necessary to maximize  $L$  given by

$$L = \sum_{i=1}^N \ln(A_i) + \sum_{i=1}^N \ln(B_i) + \sum_{i=1}^N \ln(W_i) - M, \quad (5.9)$$

where

$$M = \int A(\omega) B(\omega) W(\omega) d\omega$$

over all phase space, with respect to our parameters.

Detailed knowledge of the functional behavior of  $A(\omega)$  and  $B(\omega)$  was not required. The first two sums over  $\ln(A)$  and  $\ln(B)$  in this quantity were constants, independent of our parameters. They were, therefore, ignored (actually set to zero) in the optimization process. Evaluation of the integral  $M$  was made possible by using the entire thrown Monte Carlo sample which, after weighting as described in Sec. IV A, had a distribution  $B(\omega) \exp(-t/\tau)$  over phase space. Events which passed our cuts were assigned an acceptance  $A = 1$ , and  $A = 0$  if they failed.

In this way, we calculated

$$\begin{aligned} M &= \int A(\omega) B(\omega) W(\omega) d\omega \\ &= \frac{1}{T} \sum_{j=1}^P w_j W_j \exp(+t_j/\tau), \end{aligned} \quad (5.10)$$

where  $T$  was the sum of weights of all thrown (passing and failing) Monte Carlo events,  $P$  the number of passing Monte Carlo events, and  $w_j$ ,  $t_j$  the weight and proper time, respectively, of the  $j$ th passing Monte Carlo event. Two further complications were, first, that our data sam-

ple actually consisted of weighted events, with weights  $w$  that were negative in the background subtraction bands described in Sec. III E, and second, that the  $\Xi^-$  decay parameters  $\alpha$ ,  $\beta$ ,  $\gamma$  were not independent, but related by Eq. (5.4). In our fit, therefore, we maximized the function  $L'$  (including a Lagrange multiplier  $\lambda$ ) defined by

$$L' = \sum_{i=1}^N w_i \ln(W_i) - M + \lambda(\alpha_{\Xi}^2 + \beta_{\Xi}^2 + \gamma_{\Xi}^2 - 1)^2 \quad (5.11)$$

with respect to  $\alpha_{\Xi}$ ,  $\beta_{\Xi}$ ,  $\gamma_{\Xi}$ , and  $P_{\Xi}(x, p_T^2)$ .

### C. Polarization of $\Xi^-$

In the description in Sec. V B above, no mention was made of the fact that the parameter  $P_{\Xi}$  was, in fact, a function of  $x$  and of  $p_T^2$  for the  $\Xi^-$ . In order to make use of our full  $\Xi^-$  sample, therefore, we made two fits. In the first, (the “ $x$  fit”) we treated  $P_{\Xi}$  as if it were only a function of  $x$ , with eight possible, discrete values—one for each of eight ranges in  $x$ . We fit 11 parameters ( $\alpha, \beta, \gamma, P_{x1}, \dots, P_{x8}$ ) using the method described in Sec. V B with a value of  $P_{\Xi}$  assigned to each event based upon its placement in one of these  $x$  ranges. In the other fit (the  $p_T$  fit) a similar division into six  $p_T$  ranges was made.

In each case,  $\alpha_{\Xi}$ ,  $\beta_{\Xi}$ ,  $\gamma_{\Xi}$ , and all  $P_{\Xi}$  values were optimized. In this way, events from different  $x$  or  $p_T$  regions were all constrained to have the same values for  $\alpha$ ,  $\beta$ , and  $\gamma$ . The distributions resulting from the  $x$  fit are shown by the solid curves of Figs. 17(a)–17(d) and were obtained by weighting the Monte Carlo events by the function  $W$  defined in Eq. (5.7). Very similar curves were obtained from the  $p_T$  fit, and clearly provided an excellent description of the data. Results of these two fits are given in Table V. Polarization of hyperons produced by proton collisions in hyperon beams has been observed to grow systematically<sup>20</sup> with increasing  $p_T^2$ . This behavior has also been seen for  $\Xi^-$  produced in  $K^-p$  collisions<sup>12</sup> at 5 GeV/ $c$ , and to a lesser extent<sup>2</sup> at 8.25 GeV/ $c$ , with polarization reaching about  $(45 \pm 5)\%$  at  $p_T = 0.4$  GeV/ $c$  in the 5-GeV/ $c$  experiment. In our data, shown in Fig. 18(a) together with that from the other earlier experiments, an increase in  $P_{\Xi}$  is seen with  $p_T$ , but is somewhat more gradual than that observed in the other two experiments. A broader range of  $p_T$  values is covered in our measurements, but our polarization only reaches  $(27 \pm 7)\%$  at  $p_T = 1.5$  GeV/ $c$ . The variation which we observed in  $P_{\Xi}$  [Fig. 18(b)] also shows a general trend to increasing  $P_{\Xi}$  with increasing  $x$ . Thus, the available data seem to suggest that polarizations at large  $x$  or  $p_T$  values decrease in  $K^-p$  interactions with in-

TABLE V.  $\Xi^-$  decay fits.

Subsample $x$ range		Number of $\Xi^-$ events	Polarization (%)	$\alpha$	$\Phi$ (degrees)
Low	High				
-1	-0.5	52			
-0.5	-0.2	564	1±10	-0.55 ±1.5	13±23
-0.2	0	1259	-4±7	-0.45 ±0.08	29±75
0	0.3	3776	-12±5	-0.44 ±0.04	29±22
0.3	0.4	1454	-31±6	-0.38 ±0.06	-15±18
0.4	0.5	1292	-14±7	-0.40 ±0.07	-12±35
0.5	0.75	2268	-30±5	-0.34 ±0.05	3±14
0.75	1	759	-32±9	-0.39 ±0.07	19±19
-1	+1	11424		-0.405±0.023	5 $^{+10}_{-7}$
$p_T$ range (MeV/ $c$ )		Number of $\Xi^-$ events	Polarization (%)	$\alpha$	$\Phi$ (degrees)
Low	High				
0	115	517	4.5±11	-0.40 ±0.13	15±45
115	190	784	-4.2±9	-0.41 ±0.10	12±50
190	315	1890	-20±6	-0.46 ±0.06	15±33
315	375	924	-15±9	-0.41 ±0.08	23±18
375	850	6200	-22±3	-0.37 ±0.04	2±11
850	1500	1109	-27±7	-0.40 ±0.07	6±17
0	1500	11424		-0.404±0.024	6 $^{+8}_{-11}$
$\Xi^-$ length cut (cm)		Number of $\Xi^-$ events	Polarization (%)	$\alpha$	$\Phi$ (degrees)
	> 5	11 424		-0.40±0.02	5±8
	> 8	9066		-0.41±0.03	0±9
	> 11	7111		-0.42±0.03	6±12
	> 14	5625		-0.42±0.04	-4±16
	> 17	4435		-0.44±0.04	0±20

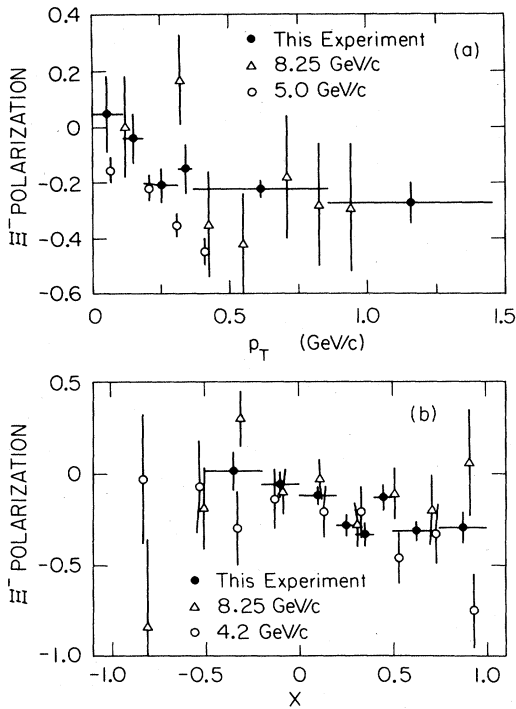


FIG. 18. Polarization of  $\Xi^-$  from  $K^-p \rightarrow \Xi^- + \text{anything}$ . (a) as a function of  $p_T$ ; (b) as a function of  $x$ . All available data from other experiments are included in the plots.

creasing beam momentum. Our data also show that the magnitude of  $P_{\Xi}$  increases with both  $p_T$  and  $x$ . This also appears to be the case for the 5-GeV/c experiment but the variation with  $x$  in the 8.25 experiment is less obvious.

#### D. Weak decay parameters

As a result of the fits described in the previous sections (VB and VC), two sets of values of  $\alpha_{\Xi}$  and  $\Phi_{\Xi}$

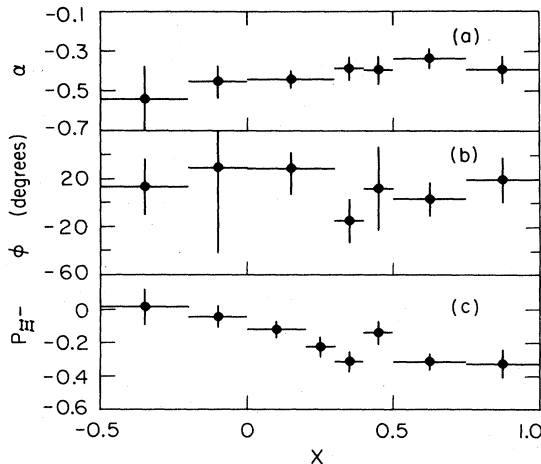


FIG. 19.  $x$  dependence of  $\Xi^-$  decay parameters. Variations in the values obtained from (a)  $\alpha$ ; (b)  $\Phi$ ; and (c) polarization are shown as functions of  $x$ . Only polarization may show any variation in the absence of systematic effects. Error bars indicate statistical uncertainties only.

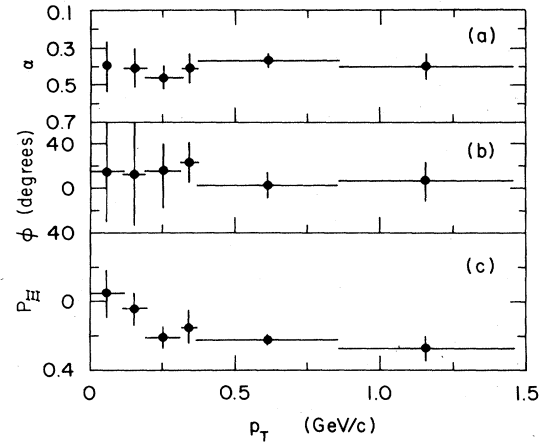


FIG. 20.  $p_T$  dependence of  $\Xi^-$  decay parameters. Variations in the values obtained for (a)  $\alpha$ ; (b)  $\Phi$ ; and (c) polarization are shown as functions of  $p_T$ . Only polarization may show any variation in the absence of systematic effects. Error bars are purely statistical.

( $=\arctan \gamma_{\Xi}/\beta_{\Xi}$ ) were obtained—one in which  $P_{\Xi}$  was regarded as a function of  $x$  and the other in which it was regarded as a function of  $p_T$ . They are presented in Table V, and are seen to be in excellent agreement.

As a test of the magnitude of systematic errors in our data, and our fitting procedure, various subsamples of events, defined in Table V, were fitted independently. For example, various length cuts were applied to examine the possibility that background might affect our results. We also made various event selections on the basis of both  $x$  and  $p_T$ . The values of  $\alpha_{\Xi}$  and  $\Phi_{\Xi}$  for these subsamples are tabulated in Table V and plotted in Figs. 19–21 as functions of  $x$ ,  $p_T$ , and the  $\Xi^-$  length cut, respectively. Obviously, agreement between subsamples is excellent and dominated by statistical errors. Included in Figs. 19 and 20 are our measurements of  $P_{\Xi}$ , and a clear correlation

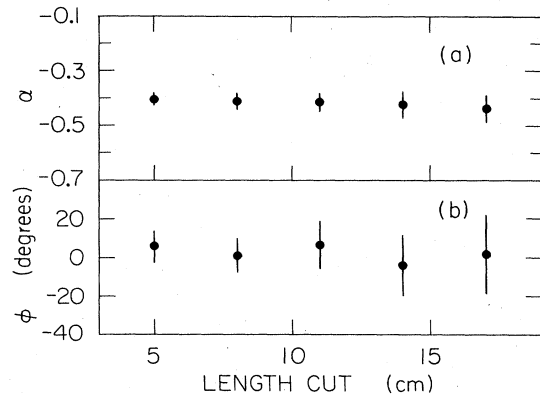


FIG. 21. Systematic effects in  $\Xi^-$  decay parameters. Variations in values obtained for (a)  $\alpha$  and (b)  $\Phi$  are shown as functions of  $\Xi^-$  track length cut. Longer length cuts reduce background contamination. Error bars represent purely statistical errors from the fits to the various samples.

TABLE VI.  $\Xi^- \rightarrow \Lambda\pi^-$  decay parameters.

Source	Approximate number of events used in fit	$\alpha$	$\Phi$ (degrees)
All experiments before Ref. 10	25 000	$-0.385 \pm 0.017$	$2 \pm 6$
BNL hyperon beam (Ref. 10)	9 046	$-0.49 \pm 0.04$	
CERN SPS hyperon beam (Ref. 11)	150 000	$-0.462 \pm 0.015$	
BNL MPS ( $K^-p$ ) (Ref. 12)	20 865	$-0.40 \pm 0.03$	$14.7 \pm 12.3 \pm 10.0$
This experiment	11 424	$-0.40 \pm 0.03$	$5 \pm 10$

can be seen between smaller uncertainty in  $\Phi_{\Xi}$  and large magnitude of  $P_{\Xi}$ . To test the sensitivity of our results to our assumptions regarding background, we also varied the weight we assigned to the  $\Xi^-$  sideband events. We varied this  $w$  in Eq. (5.11), between its limits of 0 and  $-1$  and produced a variation in  $\alpha_{\Xi}$  of 0.05 without any observable change in  $\Phi_{\Xi}$ . The value of  $-0.36$  for  $w$  which we have used, arises from our fit to the distribution of  $\Lambda\pi^-$  mass in Fig. 4, and can be adjusted by  $\pm 0.3$  at most. Including these systematic uncertainties, our best values for decay parameters (taken from the  $x$  fit, which also provided estimates of statistical uncertainties), are  $\alpha_{\Xi} = -0.40 \pm 0.03$  and  $\Phi_{\Xi} = 5 \pm 10$  degrees.

#### E. Comparison with other results

Parameters obtained from the most recent experimental measurements<sup>10-12</sup> are summarized with our own in Table VI. Values for  $\alpha_{\Xi}$  were recomputed from the ones published using the best value<sup>17</sup> for  $\alpha_{\Lambda}$  of  $0.642 \pm 0.013$  on the assumption that the product  $\alpha_{\Xi}\alpha_{\Lambda}$  should remain unchanged. Values for  $\Phi_{\Xi}$  (only measurable in experiments where  $\Xi^-$  polarization is evident) are largely unaffected by  $\alpha_{\Lambda}$  and are tabulated as quoted.

An odd discrepancy in  $\alpha_{\Xi}$  exists between the hyperon beam results and those from  $K^-p$  experiments, the former tending towards larger, negative values. A possible explanation for this discrepancy might arise from the effect of background in the  $\Xi^-$  sample referred to above. Such background events display a decay asymmetry different from that of the  $\Xi^-$ , and therefore affect the perceived value for  $\alpha_{\Xi}$ . By adjusting our assumptions regarding the amount of this background ( $w$ ) between extreme limits, we were able to alter  $\alpha_{\Xi}$  from  $-0.44$  to  $-0.39$ . However, in order to make our value agree with either of the hyperon beam results, we would have to assign a value for  $w$  greater than 1.0. This would describe an unlikely situation where rather than having a number of  $\Xi^-$  events in the dotted regions of Fig. 4, the background itself was actually enhanced exactly in the  $\Xi^-$  region. As noted above, we did adjust the actual amount of background in our sample by requiring a variety of different  $\Xi^-$  length cuts. This did not, within our model, affect our value for  $\alpha_{\Xi}$ . Most results prior to Refs. 10 and 11 came from  $K^-p$  bubble-chamber experiments where little background existed, since decay vertices could be clearly observed by human scanners. Both our experiment, and that of Ref. 12, also use  $K^-p$  induced  $\Xi^-$  samples and in both a noticeable background clearly existed. Its magnitude and effect was, however, easily modeled from the  $\Xi^-$  sidebands.

All these experiments appear to favor similar values of  $\alpha_{\Xi}$  near  $-0.40$ .

On the other hand, the experiments described in Refs. 10 and 11 obtained data from hyperon beams where the inherent assumption of no background was made. These experiments obtained values for  $\alpha_{\Xi}$  closer to  $-0.47$  with small errors from the slope of their  $\cos\psi_3$  distributions. The existence of a strongly asymmetric background in their samples, though unlikely, could explain this discrepancy.

From Table VI, we note that the uncertainty in  $\alpha_{\Xi}$  does not decrease as the square root of the number of events in the fit samples, but is ultimately limited by systematic effects, and by the uncertainty in  $\alpha_{\Lambda}$ . For instance, the two experiments with the greatest precision achieve errors within a factor of 2 from ours, since in our experiment, we experienced relatively little systematic uncertainty, and relatively good statistical precision. Our results, therefore, contribute significantly to the new world-average values for  $\alpha_{\Xi} = -0.427 \pm 0.014$  and  $\Phi_{\Xi} = (3.9 \pm 5.2)^\circ$  which can be inferred from Table VI.

#### F. The $\Delta I = \frac{1}{2}$ rule

The ratios  $\alpha_{\Xi^0}/\alpha_{\Xi^-} = 0.977$  and  $\tau_{\Xi^-}/\tau_{\Xi^0} = 0.484$  can be calculated, after allowing for phase-space factors, by assuming that the two decays

$$\Xi^0 \rightarrow \Lambda\pi^0, \quad \Xi^- \rightarrow \Lambda\pi^-$$

proceed with  $\Delta I = \frac{1}{2}$   $s$ -wave and  $p$ -wave amplitudes ( $S_1$  and  $P_1$ ) alone. Introducing the possibility of  $\Delta I = \frac{3}{2}$  amplitudes ( $S_3$  and  $P_3$ ) one obtains the ratios<sup>21</sup>

$$\alpha_{\Xi^0}/\alpha_{\Xi^-} = 0.977 + 1.37(S_3/S_1 - P_3/P_1),$$

$$\tau_{\Xi^-}/\tau_{\Xi^0} = 0.484 - 1.44S_3/S_1 - 0.06P_3/P_1.$$

Using the new world value for  $\alpha_{\Xi^-}$  computed in Sec. VE, and the best averages for  $\alpha_{\Xi^0}$ ,  $\tau_{\Xi^-}$ ,  $\tau_{\Xi^0}$  from Ref. 17 we obtain

$$S_3/S_1 = -0.058 \pm 0.015,$$

$$P_3/P_1 = -0.051 \pm 0.046,$$

indicating some violation of the  $\Delta I = \frac{1}{2}$  rule in the  $s$ -wave amplitude. We note that if we omit the large negative values for  $\alpha_{\Xi^-}$  obtained by the hyperon beam experiments the calculation above leads to

$$S_3/S_1 = -0.061 \pm 0.015 ,$$

$$P_3/P_1 = -0.119 \pm 0.046 ,$$

indicating some  $\Delta I = \frac{3}{2}$  contribution to both waves.

The major source of uncertainty in  $P_3/P_1$  arises from that in  $\alpha_{\Xi^0}/\alpha_{\Xi^-}$ . In order to establish any violation of the  $\Delta I = \frac{1}{2}$  rule in the  $p$ -wave amplitudes, better measurements of both  $\alpha_{\Xi^-}$  and  $\alpha_{\Xi^0}$  are still required.

## VI. SEARCH FOR HIGHER-MASS HYPERON STATES

Very little information on the production of strange baryons has been accumulated over the last few years. In the most recent review<sup>22</sup> in the 1980 baryon conference, it was noted that the situation of  $\Xi^*$  spectroscopy had changed little in four years and that the only well-established  $\Xi^*$  states were still the  $\Xi(1530)$ ,  $\Xi(1820)$ , and  $\Xi(2030)$ . Other narrow states had more recently been reported with masses at 1680 and 2370 MeV/ $c^2$ , but confirmation by other experiments was not yet possible. Several other  $\Xi$  states which had been reported with masses at 1630, 1940, 2240, and 2420 MeV/ $c^2$  had only been seen with a statistical significance of about four standard deviations, or less, in various bubble-chamber experiments using  $K^-$  beams with momenta less than 5 GeV/ $c$ . One of the most interesting strange-baryon states observed had been the very narrow, high-mass  $\Sigma^+(3170)$  reported<sup>23</sup> to have decay modes only to multistrange combinations of hadrons such as  $\Xi K + \pi$ 's,  $\Sigma K \bar{K} + \pi$ 's, or  $\Lambda K \bar{K} + \pi$ 's, etc. All data on these particles were obtained from bubble chambers.

Since the 1980 conference, one bubble-chamber experiment<sup>4</sup> and one  $K^-p$  counter experiment<sup>24</sup> have reported weak evidence supporting the existence of the  $\Xi(2370)$ , though the former experiment casts doubt upon its identity as a normal, single  $\Xi$  state in view of its peculiar excitation function. This and another counter experiment<sup>25</sup> using a hyperon beam have also presented some evidence in support of the existence of the  $\Xi(1940)$ , though both signals appear to be less than four standard deviations. The latter experiment observed the decay to  $\Xi^- \pi^+$ , the mode of observation of the earlier bubble-chamber experiments. The same experiment also saw evidence for  $\Xi(1680)$ , but concluded that the most likely spin-parity was  $\frac{1}{2}^+$  in contrast with the assignment of  $\frac{1}{2}^-$  tentatively made by the original authors.<sup>26</sup>

It still appears that the only confirmed  $\Xi$  states are the  $\Xi(1530)$ ,  $\Xi(1820)$ , and  $\Xi(2030)$ , and that definitive data on all the other states is still required. Given that, with the presently acquired data, our experiment is equivalent to the largest bubble-chamber experiment, it is of interest to search for these states. We find, as expected, evidence for the  $\Xi(1530)$  and  $\Xi(1820)$  which have known decay modes to  $\Xi^-$ , but do not find, as yet, conclusive evidence for other states. In particular, we do not observe the  $\Xi(1940)$ . Our data also represent the only means available to confirm the existence of the  $\Sigma^+(3170)$  which we fail to do.

### A. $\Xi^*$ states

Figure 22 shows the inclusive  $\Xi^- \pi^+$  effective-mass distribution over a wider mass range than that in Fig. 7. In this, as in all other mass plots shown here, an attempt has been made to distinguish  $\pi/K$  ambiguities using both time of flight and Cerenkov devices. It is a striking fact that, apart from the  $\Xi(1530)$ , no evidence for  $\Xi^*$  resonances is seen in Fig. 22. This plot includes all multiplicities, so a certain amount of combinatorial background exists (approximately two combinations, on average, per event). A variety of subsamples, e.g., a specific multiplicity, etc., were examined and none showed any significant signal apart from the  $\Xi^0(1530)$ . One such subsample (shaded events in Fig. 22) was chosen by selecting the  $\Xi^- \pi^+$  combination in each event for which four-momentum transfer from  $K^-_{\text{beam}}$  to  $\Xi^- \pi^+$  was smallest. The evidence presented in Sec. IV suggests that baryons with multiple strangeness appear to be produced by hyperon exchange, prompting this selection. It can be seen, however, that the  $\Xi^0(1530)$  signal diminishes in strength when this selection is made and indicates that many of the  $\Xi^0(1530)$  are probably themselves decay products of higher-mass states. Earlier experiments, mostly at lower momenta,<sup>17</sup> have reported the existence of a variety of states in this system, usually as four standard deviation effects. The positions at which such states have been reported are indicated on Fig. 22. The lack of  $\Xi^*$  states decaying to  $\Xi^- \pi^+$  is a prediction of a model of baryons based upon two-body  $qq$  color forces.<sup>27</sup> In the model, the couplings of  $\Xi^*$ 's with

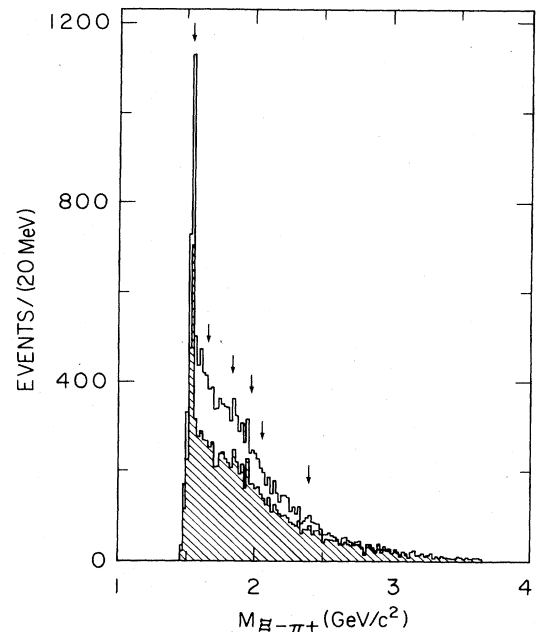


FIG. 22.  $\Xi^- \pi^+$  effective-mass distribution. All combinations in which the  $\pi^+$  has particle-identification information consistent with a  $\pi^+$  are plotted unshaded. The shaded events are those combinations (one per event) having the smallest value for  $u - u_{\text{min}}$ , where  $u$  is the four-momentum transfer from the  $K^-$  beam to the  $\Xi^- \pi^+$  system. Arrows indicate positions at which resonances in this system have been reported. The  $\Xi^-(1530)$  peak width is consistent with our mass resolution.



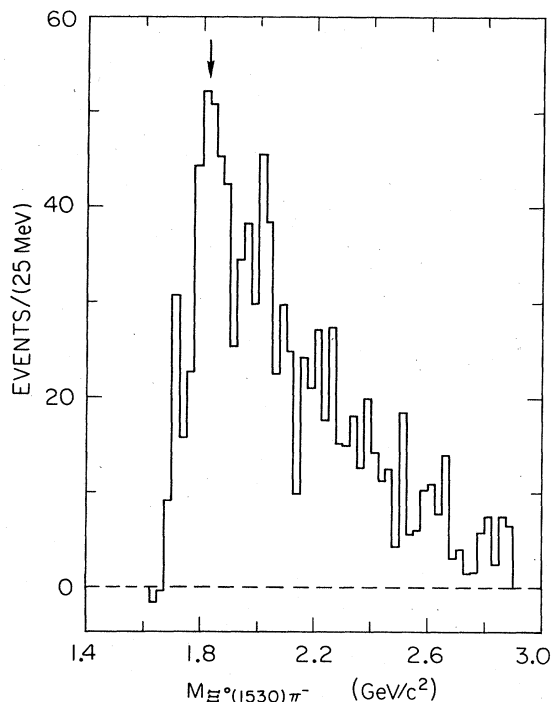


FIG. 23.  $\Xi^0(1530)\pi^-$  effective-mass distribution. All combinations are plotted. The arrow indicates the position of the  $\Xi^-(1820)$  resonance.

masses below  $2.1 \text{ GeV}/c^2$  to this “elastic” channel are expected to be small with their decays being dominated by “inelastic”  $Y\bar{K}$  modes. Our data support this picture. Our small acceptance in the higher-mass ranges of the  $\Xi^-\pi^+$  spectrum precludes the possibility of observing anything but very strong signals above  $2.1 \text{ GeV}/c^2$ .

The only other well-established state that we might expect to see in our  $\Xi^-$  channels is the  $\Xi(1820)$  which has a known decay mode to  $\Xi(1530)\pi$ . Our mass plot for the  $\Xi^0(1530)\pi^-$  system is shown in Fig. 23 (with background subtracted as outlined earlier). A clear signal is seen corresponding to the decay of the  $\Xi^0(1820)$  to  $\Xi^0(1530)\pi^-$ . No other states are seen in this decay mode.

### B. The $\Sigma^+(3170)$ Hyperon

This state is one of the most interesting hyperons to be reported, with high mass, narrow width, and unusual decay modes, yet no corroboration of its existence has been possible to date. Data in support of its discovery were originally presented jointly by two experiments<sup>23</sup> to indicate an enhancement of at least six standard deviations at  $3.17 \text{ GeV}/c^2$  with a width comparable to the resolution of the experiments involved.

The state was seen in the reaction

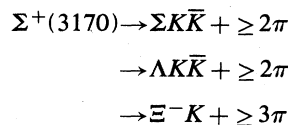


at 6.5 and 8.25 GeV/c. Its characteristics were as follows.

- (1) Mass  $3.17 \text{ GeV}/c^2$  and width compatible with zero.
- (2) Produced by baryon ( $\Delta$ ) exchange. The distribution

of the recoil  $\pi^-$  was characteristically in the backward direction in the center-of-mass system in the  $\Sigma^+(3170)$  events, while it was in the forward direction in neighboring bins.

(3) The  $\Sigma^+(3170)$  decayed only to high-multiplicity states with multiple units of strangeness:



and not, for example, simply to  $\Sigma$  or  $\Lambda$  + pions.

(4) Neither the  $\Sigma^0(3170)$  nor the  $\Sigma^-(3170)$  was seen.

The above observations were made by studying effective masses of the systems listed. Such a study cannot be made with our present data, but it is possible to use our  $\Xi^-$  data to search for the above reaction, where the  $\Sigma^+(3170)$  decays to  $\Xi^-K + \pi$ 's by investigating the missing mass recoiling against the slowest  $\pi^-$  in the subsample of events in which we require (a) a clean  $\Xi^-$ , (b) at least one  $\pi^-$ , and (c) two or more additional charged pions or kaons.

The resulting missing-mass distribution is shown in Fig. 24. This shows all events with the above criteria and with the  $\pi^-$  produced backward in the overall center-of-mass system (c.m.s.). The resolution expected in the  $\Sigma^+(3170)$  region is estimated to be less than 20 MeV, so any signal should be seen in one bin in the plot. In Fig. 24 there are five events in the 3.17-GeV bin, about the number expected from a smooth background curve drawn through the region. Using our knowledge of the acceptance for such events, this leads to an upper limit for the cross section for reaction (6.1) of  $0.07 \mu\text{b}$  (95% confidence level).

The cross section for this decay mode of the  $\Sigma^+(3170)$  was  $(0.15 \pm 0.07) \mu\text{b}$  at 8.25 GeV/c and  $0.3 \pm 0.2 \mu\text{b}$  at 6.5 GeV/c.<sup>23</sup> Extrapolation of these cross sections to 11 GeV/c for comparison with our result is obviously model dependent, and statistically uncertain as well, but two extreme cases can be considered. The most pessimistic would assume that this two-body cross section, mediated

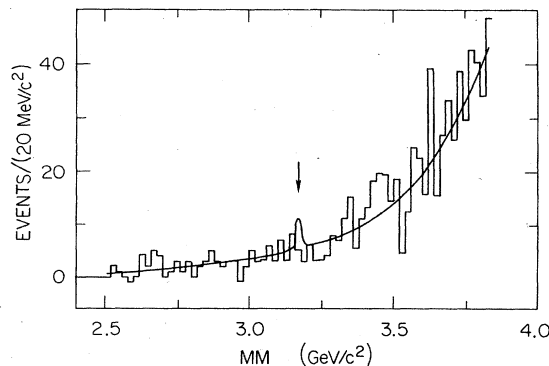


FIG. 24. Missing mass opposite the  $\pi^-$ . The event sample is as defined in the text. The curve is a Gaussian peak having a width equal to our resolution centered at  $3.17 \text{ GeV}/c^2$  plus a smooth background. The peak size is that expected from  $I = \frac{3}{2}$  (baryon) exchange.

by  $I = \frac{3}{2}$  baryon exchange, might fall with the fourth power of  $K^-$  momentum, and gives an 11-GeV/ $c$  cross section of  $0.05 \mu\text{b}$ . The most optimistic might assume that meson exchange was possible leading to a cross section of about  $0.1 \mu\text{b}$ . The appearance of the signal in the former case is illustrated, as it should appear, in Fig. 24. Clearly, our data do not support the existence of the  $\Sigma^+(3170)$ , produced with the cross sections measured in Ref. 23, but cannot rule out its existence, with production by  $\Delta$  exchange, at the 95% confidence level. Our data do exclude production of  $\Sigma^+(3170)$  by meson exchange, however.

## VII. CONCLUSIONS

From a study of  $\Xi^-, \Omega^-,$  and  $\Xi^0(1530)$  inclusive production from 11-GeV/ $c$   $K^-p$  reactions, we can conclude the following.

(i) All three particles are produced predominantly in the forward hemisphere in the c.m.s., as would be expected if produced by hyperon-exchange mechanisms, or if they were daughters of baryon states that were.

(ii) Scaling in the variable  $x$  appears to work well at our energy for all three particles.

From the  $\Xi^-$  channels we further conclude the following.

(iii) Polarizations of  $\Xi^-$  decrease in magnitude (at large

$x$  or  $p_T^2$  values) with increasing beam momentum. In most experiments, a trend in this magnitude is also to increase with both  $x$  and  $p_T$ .

(iv) A discrepancy exists amongst most recent determinations of the value for  $\alpha_{\Xi^-}$ . Hyperon-beam experiments obtain values below  $-0.45$ , but  $K^-p$  experiments obtain values closer to  $-0.40$ . Our value is  $-0.40 \pm 0.03$ . Background assumptions affect this result.

(v) Some violation of the  $\Delta I = \frac{1}{2}$  rule exists in the  $s$ -wave amplitude for  $\Xi^- \rightarrow \Lambda\pi^-$  decays. More accurate determinations of  $\alpha$  for  $\Xi^0$  and  $\Xi^-$  are needed to make conclusions for the  $p$ -wave amplitude.

(vi) We confirm the  $\Xi^0(1530)\pi^-$  decay mode for the  $\Xi^-(1820)$ .

(vii) Our data fail to confirm the existence of the  $\Sigma^+(3170)$ . We obtain an upper limit for the two-body cross section for production of  $\Sigma^+(3170)$  of  $0.07 \mu\text{b}$  (95% confidence) with subsequent decay to  $\Xi K +$  pions.

## ACKNOWLEDGMENTS

This work was supported in part by the Department of Energy under Contract No. DE-AC03-76SF00515, the National Research Council, Canada, and the Natural Sciences and Engineering Research Council, Canada, and the National Science Foundation under Grant No. PHY82-09144.

\*Present address: University of Pennsylvania, Philadelphia, PA 19104.

† Present address: CERN, CH-1211, Geneva 23, Switzerland.

‡ Present address: NASA, Ames Research Center, Mountain View, CA 94040.

§ Present address: Weizmann Institute of Science, Rehovot 76100, Israel.

\*\* Present address: Los Alamos Scientific Laboratory, Los Alamos, NM 87545.

†† Present address: Iowa State University, Ames, IA 50011.

‡‡ On leave from Nagoya University, Nagoya, Japan.

<sup>1</sup>S. N. Ganguli *et al.*, Nucl. Phys. **B128**, 408 (1977); R. J. Hemingway *et al.*, *ibid.* **B142**, 205 (1978).

<sup>2</sup>M. Baubillier *et al.*, Nucl. Phys. **B192**, 1 (1981).

<sup>3</sup>P. Sixel *et al.*, Nucl. Phys. **B159**, 125 (1979).

<sup>4</sup>J. K. Hassall *et al.*, Nucl. Phys. **B189**, 397 (1981).

<sup>5</sup>C. Louedec *et al.*, Nuovo Cimento **41A**, 166 (1977); J. M. Gago, Ph.D. thesis, University of Paris VI, 1976.

<sup>6</sup>W. Morris, Report No. ANL-HEP, C.P. 75-58 (unpublished).

<sup>7</sup>E. L. Goldwasser and P. F. Schultz, Phys. Rev. D **1**, 1960 (1970).

<sup>8</sup>S. F. Biagi *et al.*, Z. Phys. C **9**, 305 (1981).

<sup>9</sup>R. L. Cool *et al.* Phys. Rev. D **10**, 792 (1974).

<sup>10</sup>W. E. Cleland *et al.*, Phys. Rev. D **21**, 12 (1980).

<sup>11</sup>S. F. Biagi *et al.*, Phys. Lett. **112B**, 265 (1982).

<sup>12</sup>J. Bensinger *et al.*, Nucl. Phys. **B252**, 561 (1985).

<sup>13</sup>M. Bourquin *et al.*, Phys. Lett. **87B**, 297 (1979); **88B**, 192 (1979); Z. Phys. C **21**, 1 (1983); **21**, 17 (1983); **21**, 27 (1983); Nucl. Phys. **B241**, 1 (1984).

<sup>14</sup>D. Aston *et al.*, SLAC report (in preparation).

<sup>15</sup>D. Aston *et al.*, Nucl. Phys. **B247**, 261 (1984); D. Aston

*et al.*, Phys. Lett. **149B**, 258 (1984).

<sup>16</sup>Fits to mass plots were made using a Breit-Wigner form for mass peaks such as the  $\Xi^-$  (actually an approximation to a sum of Gaussian profiles of differing width). The background shape was assumed to have the form

$$f(M) = (M - M_T)^\alpha \exp[-\beta(M - M_T)],$$

where  $M_T$  is the threshold mass for the system and  $\alpha, \beta$  are fit parameters.

<sup>17</sup>Particle Data Group, Phys. Lett. **111B**, 1 (1982).

<sup>18</sup>W. Koch, reprinted in *Analysis of Scattering and Decay*, edited by M. Nolic (Gordon and Breach, New York, 1968); W. B. Teusch, S. Okubo, E. C. G. Sudarshan, Phys. Rev. **114**, 1148 (1959).

<sup>19</sup>J. Orear, Report No. UCRL-8417, 23, 1958 (unpublished).

<sup>20</sup>G. Bunce *et al.*, Phys. Rev. Lett. **36**, 1113 (1976); K. Heller *et al.*, *ibid.* **41**, 607 (1978); Phys. Lett. **68B**, 480 (1977); S. Erhan *et al.*, *ibid.* **82B**, 301 (1979); F. D. Lommano *et al.*, Phys. Rev. Lett. **43**, 1905 (1979); K. Raychaudhuri *et al.*, Phys. Lett. **90B**, 319 (1980).

<sup>21</sup>O. E. Overseth and S. Pakvasa, Phys. Rev. **184**, 1663 (1969).

<sup>22</sup>B. T. Meadows, in *Baryon 1980*, proceedings of the 4th International Conference on Baryon Resonances, Toronto, edited by N. Isgur (University of Toronto, Toronto, 1981), p. 283.

<sup>23</sup>J. Amirzadeh *et al.*, Phys. Lett. **89B**, 125 (1979); J. Kinson *et al.*, in *Baryon 1980* (Ref. 22), p. 278.

<sup>24</sup>C. M. Jenkins *et al.*, Phys. Rev. Lett. **51**, 951 (1983).

<sup>25</sup>S. F. Biagi *et al.*, Z. Phys. C **9**, 305 (1981).

<sup>26</sup>C. Dionisi *et al.*, Phys. Lett. **80B**, 145 (1978).

<sup>27</sup>N. Isgur and G. Karl, Phys. Rev. D **20**, 1191 (1979); N. Isgur, G. Karl, and R. Koniuk, Phys. Rev. Lett. **41**, 1269 (1980).